

## Article

# Geometry of Local Scour Holes at Boulder-like Obstacles during Unsteady Flow Conditions and Varying Submergence

Oliver Schlömer \*  and Jürgen Herget

Department of Geography, University of Bonn, 53115 Bonn, Germany

\* Correspondence: schloem@uni-bonn.de

**Abstract:** Local scour holes are erosional bed structures that are related to different scientific disciplines in Earth science and hydraulic engineering. Local scouring at naturally placed boulders is ubiquitous, but many competing factors make it difficult to isolate the effects of a given variable. This is especially true for local scouring at natural instream obstacles that are exposed to unsteady flow conditions in the course of flood hydrograph experiments. Experimental investigations in laboratory flumes offer the advantage that boundary conditions can be systematically varied. We present novel experimental data on the impact of the submergence ratio, hydrograph skewness, and flow intensity on local scouring at boulder-like obstacles during unsteady flow and evaluate the effect of discharge chronologies. In total, 48 flume experiments on subcritical clear-water conditions and channel degradation were performed. The experimental results reveal that local scouring dominantly occurred at the rising limb when flow depth was comparable to the obstacle size, so the obstacle was unsubmerged. The steeper the rising limb, the quicker the local scour hole matured. The experimental results are relevant for the hydraulic interpretation of local scour holes found at boulders in the field. They may be utilized as a proxy for the minimum duration of the beginning stage of a flood.

**Keywords:** local scour holes; unsteady flow; boulder; flume experiments



**Citation:** Schlömer, O.; Herget, J. Geometry of Local Scour Holes at Boulder-like Obstacles during Unsteady Flow Conditions and Varying Submergence. *Water* **2023**, *15*, 958. <https://doi.org/10.3390/w15050958>

Academic Editor: Chin H Wu

Received: 29 January 2023

Revised: 20 February 2023

Accepted: 23 February 2023

Published: 2 March 2023



**Copyright:** © 2023 by the authors. Licensee MDPI, Basel, Switzerland. This article is an open access article distributed under the terms and conditions of the Creative Commons Attribution (CC BY) license (<https://creativecommons.org/licenses/by/4.0/>).

## 1. Introduction

Local scour holes are areas of crescentic deepening in the vicinity of an instream obstacle that result from sediment mobilization due to flow separation, turbulence, and the acceleration of flow in the surroundings of the obstacle [1,2]. Due to the variety of natural and instream artificial obstructions, the phenomenon of local scouring is relevant to different scientific disciplines in Earth science and hydraulic engineering. Local scouring has been extensively investigated at hydraulic structures, such as bridge piers, groynes, spur dikes [3–6], and submarine pipelines [7,8], because of safety problems.

At these structures, engineering approaches are interested in the determination of the maximum depth of the local scour hole that likely formed after prolonged exposure to flow. In the case of a flood hydrograph, i.e., the variation in flow velocity and flow depth over time at any fixed point in space [9,10], it is known that the rising limb and peak flow have the strongest impact on local scouring, while the time to reach the maximum scour depth is usually smaller than the flood duration [11–14].

Natural obstacles, such as solitary boulders in streams, are impacted by significantly different flow conditions in the course of a flood event. During lower flows, the obstacle is unsubmerged (some portion of the obstacle protrudes above the water surface), and the flow is affected by localized flow structures (e.g., hydraulic jumps). However, at higher flows, the obstacle occupies only the lower portion of the flow depth, and the obstacle is submerged; therefore, much of the approaching flow diverges without significant flow separation or acceleration at the obstacle's base [15].

The submergence ratio, i.e., the ratio of the flow depth to the height of the obstruction, has mostly been studied in open channel flows due to interest in fish habitat structures [15], flow structures around boulders or clasts [16–19], and sediment transport [20,21].

The laboratory investigation by [17] used a cube exposed to submergence ratios = 2.0, 2.5, and 3.0 to provide further insight into flow depth–wake structure relationships. They demonstrated that, for  $2.0 \leq$  submergence ratios  $\leq 3.0$ , regions of high turbulent kinetic energy move downstream with decreasing depth and that Reynolds shear stress ( $-u'w'$ ) increases up to 50% near the top of the cube. Refs. [22,23] showed in a fluid mechanics study on low-aspect wall-mounted obstacles that a reduction in the submergence ratio significantly increases the strength of dominant vortical structures and the shedding behavior. A dominant base structure was observed in the streamwise wake at a submergence ratio = 1.0 despite it being barely detectable at submergence ratios  $\geq 2.5$ . The origin and evolution of this base structure downstream remained unanswered. While the obstacles experienced weakly symmetric shedding at an RS = 3.5, the shedding became highly antisymmetric at a submergence ratio = 1.0.

Considering sediment transport around in-stream obstacles, a laboratory study by [20,21] found that submergence-ratio-induced wake dynamics govern the sediment deposition patterns around obstacles. In an array of regularly spaced spherical obstacles in open channel flow, sediment particles (glass spheres) that were transported as a bedload were found to deposit directly behind the obstacles at a submergence ratio = 3.5, whereas, at a submergence ratio = 0.80, they deposited directly upstream of the obstacles.

Opposite to sediment trapping in the wake of an in-stream obstruction, insights into local scouring at boulder-like obstacles under varying submergence in the course of unsteady discharge are scarce. An improved understanding of these boundary conditions is useful in regard to the hydraulic interpretation of local scour holes. Especially in ephemeral dryland rivers [24,25] with no baseflow, preserved local scour holes are common features at boulders (Figure 1a). The boulders are not transported further downstream and remain part of the river landscape [26,27]. For ephemeral dryland rivers, local scouring is triggered by flash floods, i.e., a flow of water that arrives suddenly at a fixed point, changes rapidly in velocity and flow depth, and lasts a short time [28]. Herget et al. [29] used the preserved geometry of local scour holes at large boulders located in arid and ungauged basins to estimate the flow velocities of past flood events. Although plausible results could be presented, the spatiotemporal evolution of local scour holes at boulder-like obstacles during a flood hydrograph has not been experimentally investigated yet.

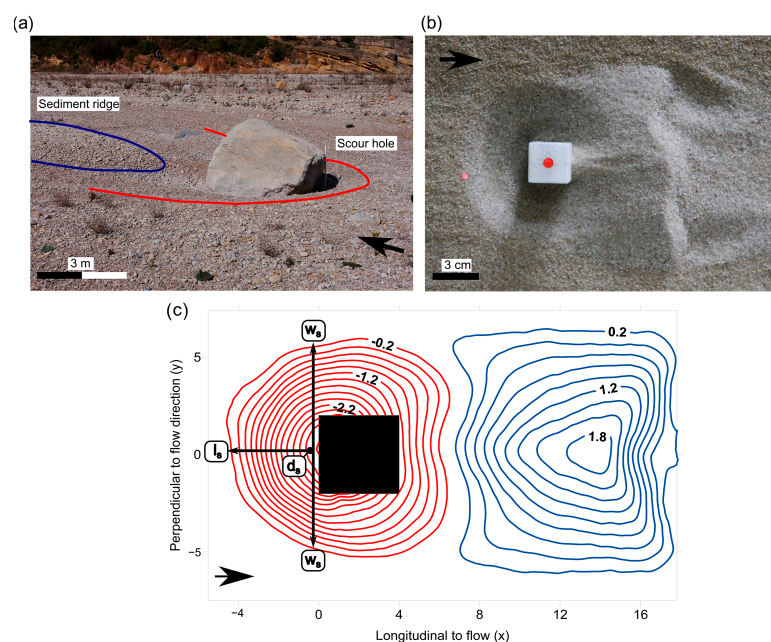


**Figure 1.** (a) Local scour hole at a boulder in ephemeral Rambla de la Viuda, NE Spain, 2019. (b) Local scour hole at a cube generated in a flume. (c) Plan view of a local scour hole at a cuboid obstacle at laboratory scale (cm) indicating local scour hole (red isolines) and sediment ridge (blue isolines). Arrows indicate direction of flow. Reprinted from Schlömer et al. [29].

Therefore, the present study experimentally investigates the impact of hydrographs of different amounts of skewness, varying durations, and different flow intensities on the enlargement processes of local scour holes at boulder-like obstacles over time. Within this context, the objectives of this contribution are as follows:

- To present experimental data on the enlargement of local scour holes at boulder-like obstacles over time that are exposed to different water levels.
- To analyze the geometry of local scour holes for unsteady discharge over time through a systematic laboratory flume study.
- To evaluate the history dependence of local scouring at a boulder-like obstruction in different hydrograph scenarios because local scouring is not independent from past flood events [30,31].

Before presenting the experimental boundary conditions and deriving the working hypothesis, a review on the geometry of obstacle marks and the turbulent flow field is presented. This study used a flume as a process-focused laboratory prototype [32] to reproduce the processes and resulting morphologies (i.e., local scour holes). Experimental hydrographs were constructed to represent the hydraulic conditions in ephemeral dryland streams, but they do not represent a specific natural prototype. Hydrographs were operationalized using dimensional parameters, including the dimensionless effective flow work.

The time-series data on local scour hole geometry revealed that local scouring dominantly occurred at the rising limb of the hydrographs when the flow depth was comparable to the obstacle size, so the obstacle was unsubmerged. Up to 80% of the scour hole size at the end of experimental runs was reached in only 10% of the experimental runtime, so the skewness of the hydrograph was an important factor.

## 2. Review on Local Scouring at Boulder-like Obstacles

### 2.1. Geometry of the Local Scour Holes

The morphology of local scour holes at boulder-like obstacles is consistent over a range of spatial scales from a small-scale laboratory ( $10^{-2}$  m) to scour holes at boulders (10 m) [33] (Figure 1a,b). The local scour hole forms at the luv side of the approaching flow upstream of the obstacle. They can be approximated to be an inverted frustum cone with an elliptical shape in plan view (Figure 1c). The geometry of a local scour hole can be characterized by certain geometrical length scales, including the local scour hole depth at the obstacle front ( $d_s$ ), measured from the undisturbed upstream bed; the local scour hole frontal length ( $l_s$ ) in the plane of symmetry to the incoming flow, measured from the obstacle frontal face to the upstream edge of the scour hole; and the local scour hole frontal width ( $w_s$ ), measured perpendicular to the direction of incoming flow from the lateral edges of the scour hole at the obstacle frontal face [34].

Deviations in the aforementioned spatial pattern are possible, as the size and shape of the boulder are of paramount importance for the local scouring process.

In the case of a boulder-like obstacle, its effective size can be described based on its height above the streambed and its width perpendicular to the direction of flow. From experimental observations, it is known that, for a given flow depth and velocity, irrespective of unsubmerged or submerged conditions, the size of a local scour hole at a boulder-like obstacle is proportional to the obstacle size [35].

Additionally, the length of the obstacle in the streamwise direction is important, as it defines the hydrodynamic shape. The hydrodynamic shape can be differentiated in stream-lined obstructions with crossflow dimensions smaller than its streamwise dimensions and in bluff obstructions with crossflow dimensions comparable to its streamwise dimensions [36]. Generally, local scouring at the obstacle front is more intense in bluff obstructions.

Moreover, boulders in streams have to be considered mobile in the sense that scouring can undermine the obstacle and induce movement that is characterized by tilting and the self-burial of the obstacle. Consequently, this process changes the boulder's exposure to flow and weakens the scouring processes [37].

## 2.2. Flow Field

If a boulder is unsubmerged, which is a condition that is analogous to scouring at bridge piers, the following processes are common: (1) an increased flow velocity lateral to the obstacle; (2) the formation of a jet-like downflow at the obstacle front due to a pressure gradient; and (3) the formation of unsteady turbulent necklace-like vortical structures at the obstacle base, commonly referred to as a horseshoe vortex system (HV) [38–41]. These processes amplify bed shear stress relative to the undisturbed upstream flow and induce sediment mobilization in the vicinity of the obstacle [42,43]. Downstream of the obstacle, the shedding of von Karman vortices is possible in unsubmerged conditions. It is likely that these shedding vortices contribute to sediment mobilization in the wake of the obstacle and that they cause local scour hole enlargement in the downstream direction [44]. However, relatively little is understood on how these streamwise vortex structures arise and what the detailed impact on the sediment transport processes is.

Because boulders are relatively squat (height  $\lesssim$  width), they become submerged during a flood, while additional vortical structures become dominant [45,46]. In submerged conditions, an arch-shaped vortex made of two lateral vortices at the obstacle's sides is present due to flow separation at the obstacle, and a vortex is located at the crest of the obstacle [47,48]. The arch-shaped vortex bends down to the bed immediately downstream of the boulder (i.e., the near-wake region) and causes a recirculation zone where some part of the flow reverses towards the obstacle [49]. As shown by [50,51], this recirculation zone can cause local scouring in the obstacle's wake instead of frontal local scouring. If the obstacle is deeply submerged, the mid-wake region (downstream of the reattachment) is characterized by interactions between laterally detached shear layers and the extended horseshoe vortex [46]. Other scenarios include the presence of a street of regularly shedding upwelling hairpin vortices originating from the pushed down arch vortex in the recirculation region [34]. In addition to the aforementioned vortices in the wake, base vortices may be formed close to the obstacle that induce an upwash on the symmetry plane of the wake, which may be important for downstream sediment transport [52–54]. At this instance, von Karman type vortex shedding does not play a significant role in the fully submerged conditions of the obstacle [55,56].

In the case of upstream local scouring, the enlargement of the scour hole and its geometry are closely related to the HV as the main driver of sediment mobilization [57,58]. Within the local scour hole, the HV actually consists of several interacting and unsteady vortices [59]. The largest and most stable vortex is denoted as the primary horseshoe vortex (HV1), which is located close to the obstacle base. Upstream, a smaller and less coherent vortex (HV2) is located within the outer region of the frontal local scour hole (Figure 2).

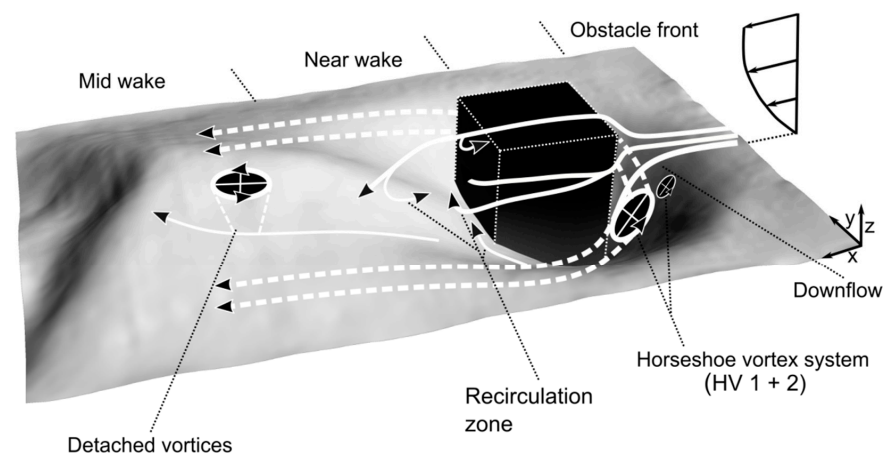


**Figure 2.** Simplified flow field in the vicinity of a submerged cuboid obstacle. Adapted from Schlömer et al. [29].

### 2.3. Enlargement Processes of Local Scour Holes

The horseshoe vortex system is responsible for the segmentation of the longitudinal local scour hole slope, originating from the obstacle front and moving to the upstream edge of the local scour hole (Figure 3). These segments consist of (1) a flat semicircular scour hole bottom ( $S_b$ ) that is closely attached to the obstacle base with a radius  $< l_s$ , (2) an inner frontal scour hole (lower slope) that is characterized by an inclination ( $\Phi$ )  $\geq$  the critical angle of repose ( $\Phi_{crit}$ ), and (3) an outer frontal scour hole (upper slope) that is characterized by  $\Phi \leq \Phi_{crit}$  [60].

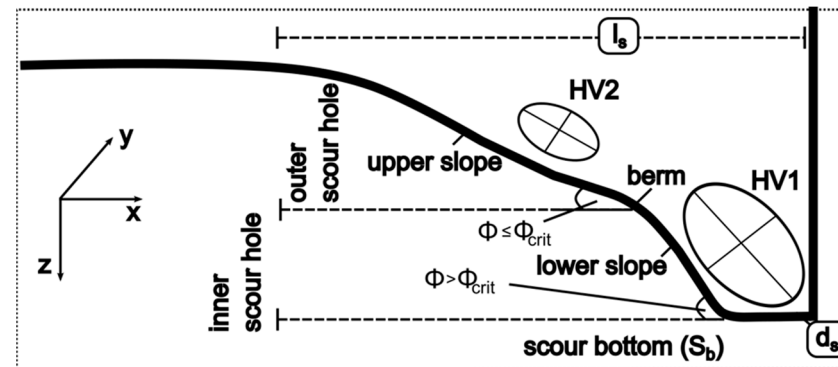


**Figure 3.** Upstream cross-sectional profile of the frontal scour hole indicating internal differentiation and positions of primary horseshoe vortex (HV1) and secondary horseshoe vortex (HV2) (not to scale). Adapted from [29].

The inner scour hole is shaped by the rotation of the HV1, which generally stabilizes the lower slope at an angle greater than the angle of repose [61]. A knickpoint in the slopes (i.e., berm) differentiates the inner and outer scour hole. However, as recently demonstrated by [62], the HV is an unsteady vortex system that randomly oscillates over time, and it, thereby, temporarily weakens due to aperiodic bimodal oscillations [63,64]. During scouring, the HV1 sinks into the frontal scour hole and extends down to  $S_b$ . The enlargement of  $l_s$  and  $w_s$  is directly related to deepening and, occasionally, to the weakening of the HV, which destabilizes the scour slopes and results in gravity mass movements.

### 2.4. Boundary Conditions

Local scouring can be interpreted as the result of a complex two-phase flow involving water and sediment that is controlled by different environmental boundary conditions comprising (1) the flow conditions, (2) the sediment characteristics, (3) the properties of the obstacle, and (4) time [65,66].

Considering a solitary solid boulder-like obstruction located in a straight, moderately sloped channel ( $<0.003$  m/m) with subcritical ( $Fr < 1$ ) flow conditions and cohesionless alluvial sediment (plane-bed type streams), local scouring can be functionally determined by

$$d_s = f(d_w, U_m, \rho, \nu, g, B, h_o, w_o, l_e, Mb, D_{50}, \rho_s, \sigma_G, U_c, d_{sed}, t, t_e) \quad (1)$$

where  $d_s$  is the local scour depth (L),  $d_w$  is the flow depth (L),  $U_m$  is the mean approach flow velocity,  $\rho$  is the water density ( $ML^{-3}$ ),  $\nu$  is the kinematic viscosity ( $L^2T^{-1}$ ),  $g$  is gravitational acceleration ( $LT^{-2}$ ),  $B$  is the channel cross section (L),  $h_o$  is the height of the obstacle (L),  $w_o$  is the obstacle width (L),  $l_e$  is the length of the obstacle (L),  $Mb$  is an indicator for the mobility of the boulder-like obstruction due to it tilting into the scoured depression (-),  $D_{50}$  is the median grain diameter of the bed sediment (L),  $\rho_s$  is the sediment density ( $ML^{-3}$ ),  $\sigma_G$  is the gradation coefficient of the sediment ( $D_{84}/D_{16}^{1/2}$  (-)),  $U_c$  is the critical mean approach flow velocity for the entrainment of the bed sediment ( $LT^{-1}$ ),  $d_{sed}$  is the thickness of the bed layer (L),  $t$  is time (T), and  $t_e$  is the time scale to reach equilibrium (T).

For noncohesive alluvial sediments (i.e., sand and gravel), equilibrium conditions are typically reached in an order of days [67–69]. However, it is well established that, for steady discharge, 80% of the local scour hole size in equilibrium conditions is reached within only 5–40% of the time to equilibrium, mainly depending on the flow velocity and grain size [70].

In Equation (1), 16 independent variables (denoted as  $n$ ) in 3 basic dimensions (denoted as  $m$ ) define the problem’s inherent degrees of freedom [71]. According to the  $\Pi$ -theorem, Equation (1) can be reduced to  $n - m$  nondimensional parameters.

To account for squat obstacles in unsubmerged and submerged conditions, the obstacle height ( $h_o$ ) and width ( $w_o$ ) are used to define the effective obstacle size ( $L_o = h_o^\alpha w_o^\beta = h_o^{2/3} w_o^{1/3}$ ), with  $\alpha + \beta = 1$ .  $L_o$  is used as a reference length scale ( $L$ ), while the exponents were derived from a data analysis presented in [35] and [69]. Assuming a constant relative sediment density  $(\rho_s - \rho)/\rho$ , i.e., neglecting  $\rho$  and  $\rho_s$  among other expressions, one obtains

$$d_s/L_o = f(d_w/L_o, U_m/g \times L_o^{1/2}, U_m/U_c, U_m \times L_o/\nu, L_o/B, Sh, M_b, L_o/D_{50}, \sigma_G, d_{sed}/L_o, t/t_e) \tag{2}$$

where  $d_s/L_o$  is the nondimensional scour depth;  $d_w/L_o$  is the submergence ratio;  $U_m/U_c$  is the flow intensity;  $U_m/g \times L_o^{1/2}$  is the obstacle Froude number ( $Fr_o$ );  $U_m \times L_o/\nu$  is the obstacle Reynolds number ( $Re_o$ );  $L_o/B$  is the blockage ratio;  $Sh (L_o/le_o)$  describes the shape of a body where, for  $Sh \leq 0.5$ , the obstruction is bluff, while, for  $Sh \geq 0.8$ , the obstacle is more streamlined;  $L_o/D_{50}$  is the relative sediment coarseness; and  $d_{sed}/L_o$  is the relative thickness of the bed layer, with  $L_o$  representing the size above the sediment bed ( $d_{sed}$ ). For  $d_{sed}/L_o < 1$ , the sediment layer is too thin, and  $d_s$  incision is significantly limited. Meanwhile, the slight enlargement of  $w_s$  and  $l_s$  can be observed [29]. If  $d_{sed}/L_o = 0$ , the formation of obstacle marks into a sedimentary structure is inhibited.  $t/t_e$  is the nondimensional time scale to reach equilibrium, and it is a function of  $d_w/L_o$ ,  $U_m/U_c$ , and  $L_o/D_{50}$  [70].

While Equation (2) applies to steady flow, [13] proposed the dimensionless effective flow work ( $W^*$ ) to be the generalization of the flow intensity concept to unsteady flow conditions at unsubmerged cylindrical bridge piers:

$$W^* = \int_0^{t_{end}} \frac{1}{t_{end}} \left( \frac{U_m}{U_c} - 0.5 \right)^3 \delta dt \tag{3}$$

where  $t_{end}$  is the hydrograph duration and where  $\delta$  is the Dirac delta function:

$$\delta \begin{cases} 0 & \frac{U_m}{U_c} < 0.5 \\ 1 & \frac{U_m}{U_c} \geq 0.5 \end{cases} \tag{4}$$

### 3. Working Hypothesis

It is hypothesized that, in unsteady flow conditions, at a given obstacle size, obstacle shape, and sediment size, the size of the local scour hole over time would be impacted by the degree of submergence of the obstacle. Furthermore, the skewness of the hydrograph and its overall duration are supposed to have an effect on the size of the local scour hole over time.

By neglecting the constant boundary conditions of the experiments ( $L_o/B = 0.09$ ,  $L_o/D_{50} = 40$ ,  $\sigma_G < 1.3$ ,  $d_{sed}/L_o = 1.83$ , no mobility of the obstacle, single obstacle shape) and by neglecting the viscous effects at the obstacle (i.e., dropping  $U_m \times L_o/\nu$ ) [72] as well as by considering only subcritical flow conditions at the obstacle irrespective of the flow depth (i.e., dropping  $U_m/g \times L_o^{1/2}$ ), Equation (3) is integrated into Equation (2), which leads to

$$d_s/L_o = f(d_w/L_o, W^*, t/t_e) \tag{5}$$

By assuming the shape similitude of the local scour hole, the nondimensional scour depth ( $d_s/L_o$ ) in Equation (5) can be replaced with the nondimensional scour length ( $l_s/L_o$ ) or the nondimensional scour width ( $w_s/L_o$ ) [33].

However, the validity of  $W^*$  has not been tested experimentally for the case of local scouring at squat boulder-like obstacles at different extents of submergence. Ref. [11] proposed the relationship between the normalized scour hole depth and  $W^*$  at unsubmerged cylindrical bridge piers to be

$$d_s/L_o = 0.0075 (1 - e^{-0.097 W^{*0.38}}) \quad (6)$$

The present experimental results are compared to Equation (6), although it was originally determined based on experimental runs on bridge pier models that had different boundary conditions.

## 4. Experimental Design and Procedures

### 4.1. Flume Set-Up

Experiments were conducted in a 5 m long, 0.32 m wide, and 0.27 m deep straight rectangular flume that was entirely filled with a 5.5 cm thick layer ( $d_{sed}$ ) of uniform sand ( $\sigma_G < 1.3$ ) with median grain diameter ( $D_{50} = 0.75$  mm) (Figure 4). The bottom slope of the flume was not adjustable, as it was fixed to a moderate slope (0.003 m) to ensure water flow in the flume. Within the working section (~2.7 m downstream of the inlet), subcritical flow conditions (Froude number ( $Fr = U_{m/g} * d_w^{1/2}$ ) ranging from 0.29 to 0.56) were present at any stage of the hydrograph and at any water depth. The Reynolds number ( $Re = U_m * d_w / \nu$ ) was  $\gg$  than 500 for any stage of the hydrograph, indicating turbulent flow. Discharge was controlled with a recirculating pump (Lowara FCE Series<sup>®</sup>, Langenhagen, Germany) regulated manually by two cone valves and was measured with a magnetic-inductive discharge meter (Schwing MS 1000<sup>®</sup>, Neukirchen-Vluyn, Germany, accuracy  $\pm 1\%$  of actual discharge). Flow depth ( $d_w$ ) was adjusted with a tailgate at the downstream end of the flume outlet. In order to reduce turbulence and to condition flow, a self-made flow straightener made of bundled pipes (approx. 100 pipes, diameter of 3 cm, length of 40 cm) was installed in the flume inlet.

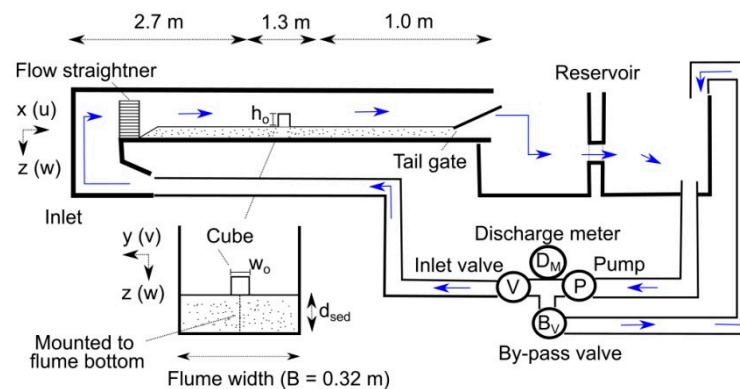


**Figure 4.** Sketch of the flume with discharge-controlling system (arrows indicate direction of flow).

A cube ( $L_o = 3$  cm) was used to represent the hydrodynamic shape of a bluff instream obstacle whose crossflow dimensions were comparable to its streamwise dimensions. The authors are aware that the shape of a cubic boulder is unlikely in natural conditions. However, the cube was supposed to represent a maximum angular obstacle for which scouring processes would be intensified.

The cube was mounted to the flume bottom to prevent tilting due to scouring, which limited further evolution of local scouring and induced equilibrium conditions more quickly.

### 4.2. Laboratory Hydrographs

Hydrographs were constructed to simulate hydrological conditions that are likely in ephemeral dryland streams (i.e., no baseflow and relatively short duration) [73]. Unsteady

discharge was simulated through a quasi-steady approach by applying the principle of stepped hydrographs, i.e., a sequence of constant discharges acting during defined intervals, which is commonly used to imitate varying discharge in flumes [74–76].

Four simply shaped single-peaked hydrographs were designed by varying the duration of rising limb ( $t_r$ ), falling limb ( $t_f$ ), and peak flow ( $t_{peak}$ ). Symmetrical ( $t_r/t_f = 1$ ), positively skewed ( $t_r/t_f < 1$ ), negatively skewed ( $t_r/t_f > 1$ ), and flash flood hydrographs ( $t_r/t_f \ll 1$ ) were constructed through this procedure. The hydrographs were made of  $n = 13$  intervals of constant discharge: 6 on the rising limb, 1 at peak flow, and 6 on the falling limb (Figure 5).

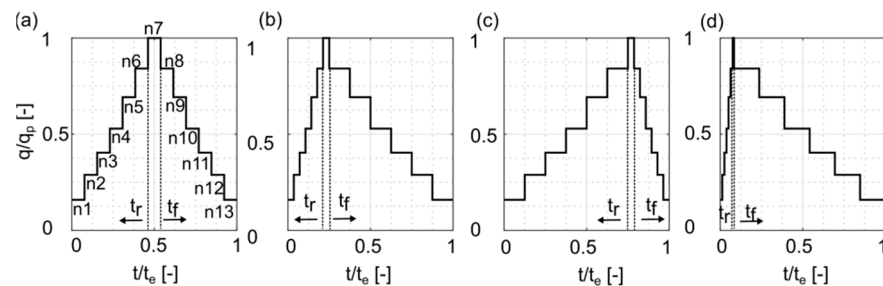


**Figure 5.** Laboratory hydrographs and indication of discharge intervals ( $n$ ) and duration of rising limb ( $t_r$ ) and falling limb ( $t_f$ ): (a) symmetrical, (b) positively skewed, (c) negatively skewed, and (d) flash flood.

For each hydrograph shape, three different experimental configurations (Series A, B, and C) were conducted in which the overall hydrograph duration ( $t_{end}$ ) was different. Through this, the dependence of local scouring on time was evaluated.

For Series A,  $t_{end}$  equaled 480 min; for Series B,  $t_{end}$  was 210 min; and for Series C,  $t_{end}$  was 120 min, with  $t_{end} = t_r + t_{peak} + t_f$ . Therefore, experimental runtime of hydrographs was not designed to define any equilibrium condition for local scouring. The runtime of each discharge interval varied between different hydrograph shapes. An overview on the individual runtime of discharge intervals for each hydrograph shape is provided in Appendix A (Table A1).

For comparison, experimental runs at constant discharge and at peak flow (i.e.,  $d_w = 8$ , obstacle fully submerged) were performed at different mean flow velocities (i.e.,  $U_m = 0.26 \text{ ms}^{-1}$ ,  $0.32 \text{ ms}^{-1}$ , and  $0.37 \text{ ms}^{-1}$ ), and they lasted 480 min. In total, 48 experimental runs were performed.

The hydrograph started from a drained flume (i.e., no baseflow). In the rising and falling limbs of the hydrographs,  $d_w$  linearly increased from 2 cm to  $d_w = 8$  cm at peak flow. In the falling limb,  $d_w$  decreased to 2 cm again, producing different degrees of submergence at the obstacle that were classified based on the deformation of the water surface profile.

In unsubmerged conditions ( $0 < d_w/L_o \leq 1$ ), the obstacle top was above the water surface, and a bow wave at the obstacle front could be detected. Meanwhile, in mid-to-far wake, irregularities of the water surface indicated the presence of trailing vortices due to detached shear layers. Unsubmerged conditions were present at the beginning of the rising limb (i.e., interval n1 and n2) as well as at the end of the falling limb (i.e., n12 and n13) (Figure 6a).

With shallow submergence, the obstacle top was only slightly below the water surface, causing the water level to drop above the obstacle top while a bow wave piled up at the obstacle front (i.e., n3 and n4 of the rising limb and n10 and n11 of the falling limb) (Figure 6b).

In fully submerged conditions ( $d_w/L_o \geq 2$ ), no disturbance of the water surface profile could be observed, indicating a free flow of the approaching boundary layer above the obstacle top (i.e., n5 and n6 of the rising limb, n8 and n9 of the falling limb, and n7 at peak flow) (Figure 6c). However, an arch-shaped vortex might be present at the obstacle's crest

and its near-wake region. The water surface profile in the working section was measured using an ultrasonic distance meter (Mic + 25, Microsonic®, accuracy ± 0.1 mm).

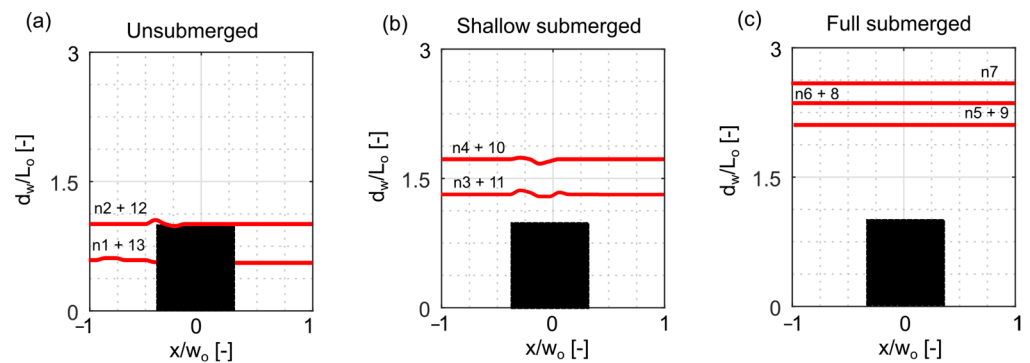


**Figure 6.** Extent of submergence of the obstacle and indication of discharge interval (n): (a) unsubmerged, (b) shallowly submerged, and (c) fully submerged.

Three different hydraulic scenarios were applied in Experimental Series A, B, and C. By increasing  $U_m$  at a given  $d_w$ , different flow intensities ( $U_m/U_c$ ) were established. For Scenario 1, clear-water conditions ( $U_m/U_c < 1$ ) prevailed during the hydrographs; for Scenario 2, flow intensity was close to general sediment mobilization ( $U_m/U_c \cong 1$ ); and, for Scenario 3, general sediment mobilization was present during the entire hydrograph ( $U_m/U_c > 1$ , general sediment movement). The hydraulic boundary conditions of the experimental series are displayed in Table 1.

**Table 1.** Hydraulic boundary conditions of flow intervals used to design hydrographs.

Interval (n)	Scenario 1 <sup>a</sup>				Scenario 2 <sup>b</sup>		Scenario 3 <sup>c</sup>	
	$d_w$ (m)	$U_c$ <sup>d</sup> (ms <sup>-1</sup> )	$U_m$ (ms <sup>-1</sup> )	$q$ (m <sup>2</sup> s <sup>-1</sup> )	$U_m$ (ms <sup>-1</sup> )	$q$ (m <sup>2</sup> s <sup>-1</sup> )	$U_m$ (ms <sup>-1</sup> )	$q$ (m <sup>2</sup> s <sup>-1</sup> )
1 + 13	0.02	0.248	0.165	$3.35 \times 10^{-5}$	0.20	$4.06 \times 10^{-5}$	0.25	$5.07 \times 10^{-5}$
2 + 12	0.03	0.268	0.20	$6.09 \times 10^{-5}$	0.22	$6.70 \times 10^{-5}$	0.27	$8.22 \times 10^{-5}$
3 + 11	0.04	0.282	0.21	$8.53 \times 10^{-5}$	0.24	$9.75 \times 10^{-5}$	0.29	$1.17 \times 10^{-4}$
4 + 10	0.05	0.293	0.22	$1.11 \times 10^{-4}$	0.26	$1.32 \times 10^{-4}$	0.31	$1.57 \times 10^{-4}$
5 + 9	0.06	0.302	0.24	$1.46 \times 10^{-4}$	0.28	$1.70 \times 10^{-4}$	0.33	$2.01 \times 10^{-4}$
6 + 8	0.07	0.316	0.25	$1.77 \times 10^{-4}$	0.30	$2.13 \times 10^{-4}$	0.35	$2.48 \times 10^{-4}$
7	0.08	0.327	0.26	$2.11 \times 10^{-4}$	0.32	$2.60 \times 10^{-4}$	0.37	$3.00 \times 10^{-4}$

Note(s): <sup>a</sup> Series A/B/C 1, 4, 7, and 10. <sup>b</sup> Series A/B/C 2, 5, 8, and 11. <sup>c</sup> Series A/B/C 3, 6, 9, and 12. <sup>d</sup> Calculation provided in Appendix A.

### 4.3. Experimental Procedure

Each experiment started by adjusting the discharge per unit width ( $q$ ) and  $d_w$  to the first interval of the hydrograph (n1). Afterwards, the obstacle was placed in the working section in the plane of symmetry to minimize sidewall effect [77]. The sediment surface in the entire flume was leveled to a flat-bed surface. Experimental runtime started at  $t = 0$  min after the cube was installed.

Between the intervals, in the rising limb, the tailgate was raised 1 to 2 cm to interrupt local scouring while  $q$  was adjusted via the cone valves of the pump to the next interval. In the falling limb, first,  $q$  was decreased while the tailgate was lowered to the corresponding  $d_w$ . Adjustments of  $q$  and  $d_w$  took approximately 3 to 5 min and were done manually. The time of adjustment was not considered to be part of experimental runtime, as local scouring was interrupted.

Although the cone valves were operated manually, the standard error of the actual discharge was less than  $9.0 \times 10^{-6} \text{ m}^2\text{s}^{-1}$ , i.e., less than 3% of the desired discharge. Thus, it was argued that desired hydrographs depicted in Figure 3 were representative of actual laboratory conditions.

During experimental runs, the sizes of  $d_s$ ,  $l_s$ , and  $w_s$  were measured with two LED distance meters (Welotec® OWRB Series, Laer, Germany, accuracy  $\pm 0.5 \text{ mm}$ ), measuring  $x$ - and  $y$ -coordinates in a local Cartesian coordinate system, with  $x$  = longitudinal as well as streamwise direction and  $y$  = horizontal, perpendicular to streamwise direction. A laser distance meter (Baumer Electric® ODAM S14C, Fraunfeld, Switzerland, accuracy  $\pm 1.5 \text{ mm}$ ) was used to measure the vertical coordinate ( $z$ ). All sensors were mounted on a traversing system on top of the flume operating in  $x$ -/ $y$ -planes. The elevation of the initial flat bed in front of the obstacle at  $t = 0 \text{ min}$  was used as reference (i.e.,  $x_0/y_0/z_0 = 0/0/0$ ).

For Series A,  $d_s$ ,  $l_s$ , and  $w_s$  were measured every third minute for each hydrograph interval. Irrespective of time, the spatial extent of  $l_s$  and  $w_s$  was determined by  $z_0 < 0$ . For Series B and C, the measurement frequency was relaxed to one and two minutes in order to generate sufficient data on each hydrograph step.

Measurements of the geometrical length scales were interpreted as quasidynamic observations because they were measured while water was flowing [78]. Thus, measurements of the  $z$ -coordinate ( $d_s$ ) were biased due to refraction of the laser beam within the water column. In absence of suspension of sediment, a simple calibration method (i.e., compensation for the travel time of light in water) was applied that yielded sufficiently accurate results when compared to measurements in drained conditions with the same measurement system. The error was less than two times  $D_{50}$ .

Additionally, the geometry of the local scour hole was measured using 2D longitudinal cross sections, i.e., streamwise direction ( $x$ -/ $z$ -coordinates) and perpendicular to streamwise direction ( $y$ -/ $z$ -coordinates) (Figure 1a, solid lines). The longitudinal cross sections were used to estimate the volumetric bedload transport rate. Cross sections were surveyed every 20 min of experimental runtime up to  $t_{\text{end}}$ .

## 5. Results and Discussion

### 5.1. Local Scour Evolution

Irrespective of the hydraulic scenario or hydrograph shape, local scouring immediately started at interval  $n_1$  of the hydrographs after placing the obstacle in the working section. Two initial depressions formed at the lateral edges of the cube front that merged to a conical scour hole in front of the obstacle ( $t \leq 1 \text{ min}$ ). The position of the maximum scour depth then migrated from the lateral sides to the obstacle front. The eroded material was deposited downstream in the wake of the obstruction as a sediment ridge with an orientation parallel to the flow direction.

During this time, the obstacle was unsubmerged, and the observed processes were analogous to the processes reported in the experimental research on bridge pier scouring [79]. With increasing experimental runtimes, the incision of  $d_s$  slowed down and asymptotically approached its maximum value at  $t_{\text{end}}$  irrespective of the hydrograph shape or hydraulic scenario (Figure 7).

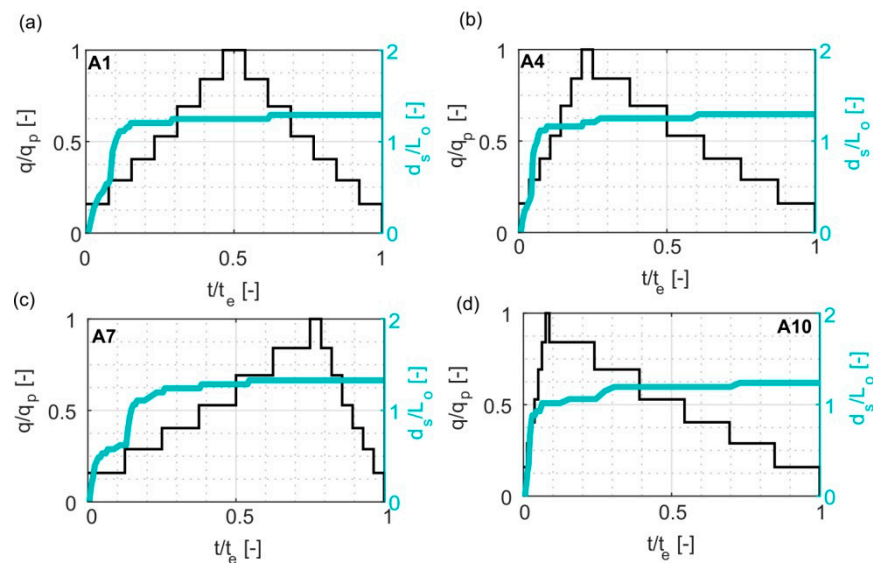


**Figure 7.** Evolution of normalized scour depth ( $d_s/L_o$ ) over nondimensional time ( $t/t_e$ ) for different hydrograph shapes in Series A experiments: (a) symmetrical, (b) left-skewed, (c) right-skewed, (d) flash flood.

#### 5.1.1. Impact of Submergence

At hydrograph interval n2,  $d_w$  was equal to  $L_o$ , which intensified local scouring. The scour hole significantly deepened as well as lengthened and widened, while the sediment ridge flattened, widened, and elongated in the downstream direction. The intensification of the local scouring processes at  $d_w/L_o = 1$  was attributed to a high pressure gradient at the obstacle front creating an intense downflow and an erosive HV system at the obstacle base. Despite the relatively short flume length, it is argued that a characteristic boundary layer profile was present for all the intervals of the hydrographs.

With increasing submergence in the rising limb of each hydrograph (i.e., intervals n3 and n4), local scouring was reduced. At hydrograph intervals n6 and n7 (peak flow), the obstacle was fully submerged ( $d_w/L_o \geq 2$ ), and local scouring was considerably reduced compared to  $d_w/L_o = 1$ . This was attributed to the fact that (i) the majority of the approaching boundary layers flow over the obstacle and that the downflow ceases and to the fact that (ii) the size and strength of the HV system is reduced in submerged conditions as outlined by [80–82].

The presence of base vortices in the wake of the obstacle in fully submerged conditions could not be verified with the present experimental setup. However, the HV system could be observed at the obstacle base due to the saltating movement of the sediment grains within the local scour hole bottom ( $S_b$ ).

The peak flow did not significantly contribute to the local scour hole size, as the obstacle was fully submerged during peak flow. Therefore, the present experimental results differ from observations reported on local scouring at bridge piers during hydrograph experiments [83–85]. Here, the obstacle was unsubmerged during peak flow, while the flow depth and velocity were considerably high. Thus, the approaching flow generated an intense downflow at the bridge pier's frontal face and an effective HV system at the obstacle base that favored scouring and vice versa.

Considering the dimensionless flow work ( $W^*$ ),  $W^*$  varied between the individual runs depending on the hydrograph shape and hydraulic scenario. For Series A experiments,  $W^*$  ranged from 1308 (clear water) to 28,382 (live bed) (Figure 8).

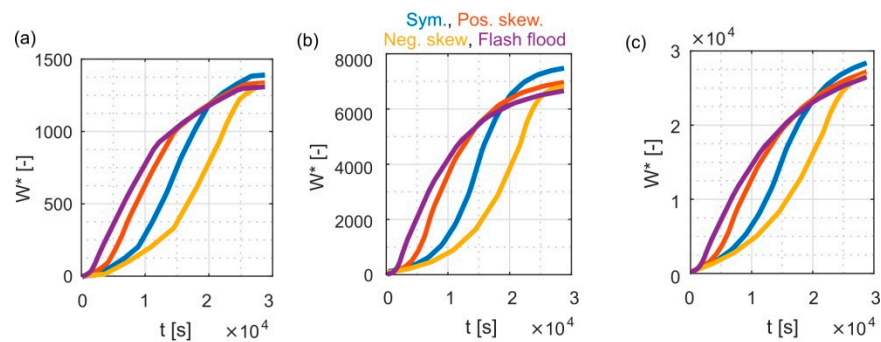


**Figure 8.** Dimensionless flow work ( $W^*$ ) of Series A experiments: (a) scenario 1 (clear water), (b) scenario 2 (transitional), and (c) scenario 3 (channel degradation).

The dimensionless scour hole depth ( $d_s/L_o$ ) was proportional to  $W^*$  as exemplified by the experimental runs on symmetrical hydrographs (A1, C1, and A1 constant) in clear-water conditions (Figure 9). However, the experimental results do not fit Equation (6) perfectly. This was attributed to the fact that a bluff angular obstacle was exposed to flow depths that were comparable to the obstacle size, which caused deeper scour holes at the beginning stages of the hydrographs prior to peak flow at  $W^* \approx 750$ . Moreover, the asymptotical trend of the enlargement of the scour depth at peak flow and during the first stages in the falling limb was attributed to the impact of the fully submerged conditions on the obstacle.

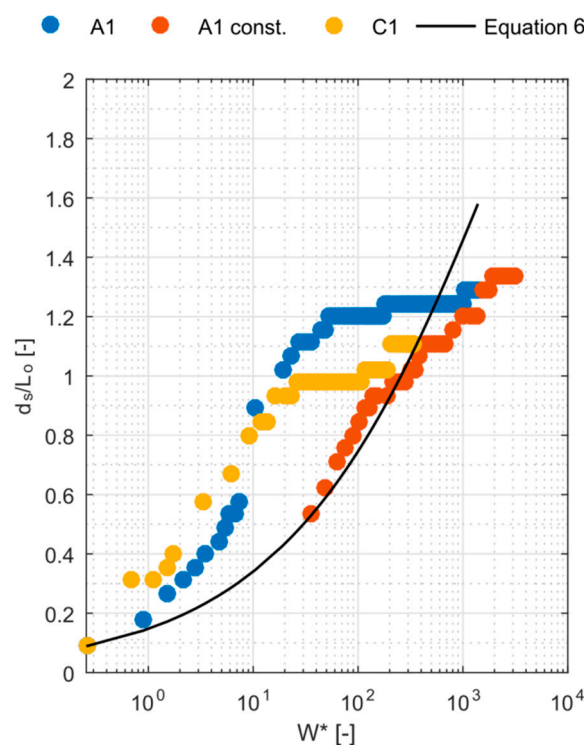


**Figure 9.** Dimensionless scour hole depth ( $d_s/L_o$ ) versus dimensionless flow work ( $W^*$ ) observed in symmetrical hydrographs of different durations in clear-water conditions.

The size of  $d_s/L_o$  at  $t_{end}$  was comparable between A1 and the constant A1 run, which highlights the importance of time in local scouring. This became obvious in hydrograph C1, as the overall duration was reduced to 25% compared to Series A, which resulted in a 12% smaller dimensionless local scour hole depth irrespective of the hydrograph shape (Figure 9, orange dots).

### 5.1.2. Impact of Hydrograph Shape

Local scouring for different hydrograph shapes in clear-water conditions showed an asymptotic evolution over time. The enlargement of the local scour depth occurred in the rising limb ( $t_r$ ) prior to peak flow ( $q_p$ ) irrespective of the hydrograph shape, while substantial enlargement in the falling limb ( $t_f$ ) was negligible (Figure 10, blue dots).

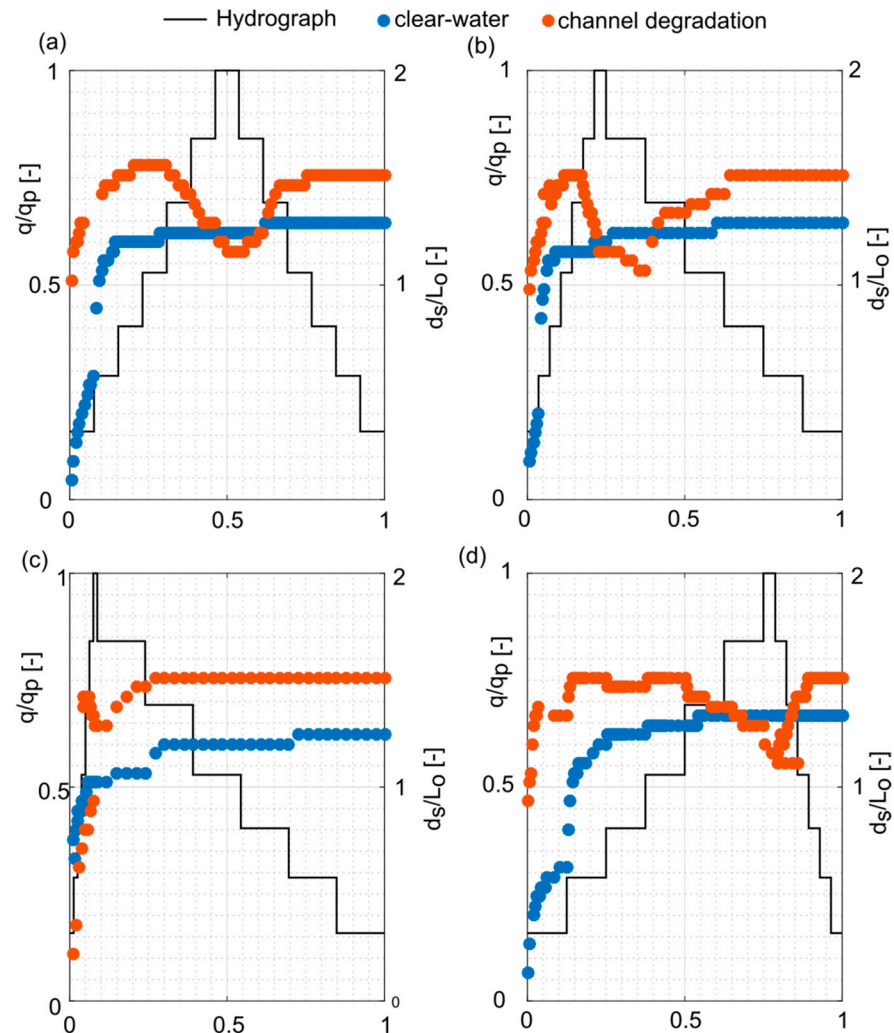


**Figure 10.** Trajectory of dimensionless scour hole depth ( $d_s/L_o$ ) versus dimensionless time ( $t/t_e$ ) for general sediment transport and clear-water conditions in Series A experiments and for different hydrograph shapes: (a) symmetrical, (b) positively skewed, (c) flash flood, and (d) negatively skewed.

For the Series A experiments ( $t_{end} = 480$  min), irrespective of the hydrograph shape,  $d_s/L_o$  already reached 76% of its size by  $t_{end}$  at  $t/t_{end} = 0.1$ . However, the skewness of the hydrograph ( $t_r/t_f$ ) affected local scouring over time. For the negatively skewed hydrograph ( $t_r/t_f = 3.53$ ) of the Series A experiments, 99% of  $d_s/L_o$  at  $t_{end}$  was reached during  $t_r$  and prior to  $q_p$  (Figure 10d), while, for the flash flood hydrograph ( $t_r/t_f = 0.08$ ), 82% of  $d_s/L_o$  at  $t_{end}$  was reached during  $t_r$ , which corresponded to 7.5% of the duration of  $t_e$ .

This observation is supported by the two extremums of the investigation (Series B,  $t_{end} = 210$  min). For  $t_r/t_f = 0.05$ , 69% of  $d_s/L_o$  at  $t_{end}$  was reached during  $t_r$ , while, for  $t_r/t_f = 7.06$ , 99% of  $d_s/L_o$  at  $t_{end}$  was reached during  $t_r$  and prior to reaching  $q_p$ . Thus, it can be stated that, the steeper  $t_r$  (i.e., positively skewed), the quicker  $d_s$  achieves a size comparable to its final size for a given hydraulic condition and experimental runtime, which coincides with the experimental results on the time evolution of  $d_s$  at bridge piers during hydrograph experiments [86,87].

The superimposition of  $d_s/L_o$ , i.e., the memorization of the previous scour depth is present for all the hydrograph shapes. This has been also documented by [88] for experiments on scouring at bridge piers during unsteady flow. The size of  $d_s/L_o$  at  $t_{end}$  was similar irrespective of the hydrograph shape or experimental series as indicated by a relative standard deviation of 0.0282, which is consistent with the observations reported by [11] on bridge pier scouring.

### 5.1.3. Impact of Flow Intensity

Local scour evolution was different for general sediment transport ( $U_m/U_c > 1$ ) in a degrading channel (Figure 10, orange dots). In the rising limb of the hydrographs, the local scour holes were larger when compared to clear-water conditions, which can be attributed to two facts:

- (i) Due to higher flow velocities at flow depths  $d_w/L_o \leq 1.5$ , the HV system could more effectively mobilize the sediment particles at the local scour hole bottom;
- (ii) The sediment output out of the local scour hole was greater than the sediment input from upstream.

The second fact especially is in accordance with previous findings reported for bridge pier scouring [89]. In this regard, it is necessary to indicate that no sediment feeding at the upstream part of the flume was conducted. Thus, the experimental setup has to be considered a degrading channel.

At peak flow, the sediment input from upstream reached its maximum, and the downstream migrating bedload sheets approached the local scour hole and partially refilled and buried it, which was indicated by a reduction in all the geometrical length scales (i.e.,  $d_s/L_o$ ,  $l_s/L_o$ , and  $w_s/L_o$ ). At the same time, the sediment output of the scour hole was reduced due to the weak erosive capacity in fully submerged conditions.

The skewness of the hydrographs controlled the amount of the refilling of the scour hole. For  $t_r/t_f = 0.08$  at  $q_p$ ,  $d_s/L_o$  was reduced by 9% compared to its prior maximum value. For  $t_r/t_f = 3.53$  at  $q_p$ ,  $d_s/L_o$  was reduced by 26% compared to its prior maximum value due to a larger timespan of sediment input into the local scour hole.

The amount of bedload ( $q^b$ ) that was transported out of the frontal local scour hole along its longitudinal axis ( $l_s-d_s$ , Figure 3) was also estimated based on two consecutive frontal scour cross sections over time by calculating the line integral (Figure 11).

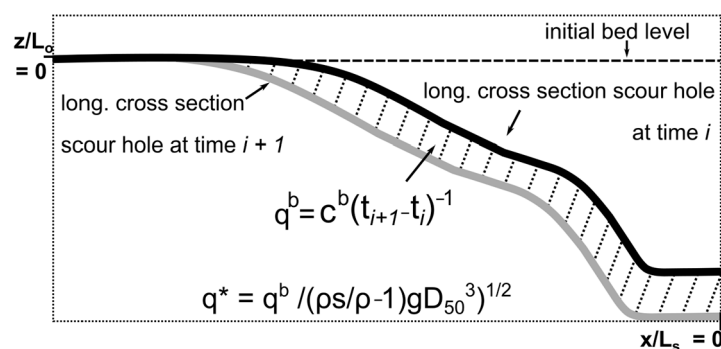


**Figure 11.** Estimation of bedload transported out of the local scour hole along its longitudinal axis ( $l_s-d_s$ , Figure 1c).

Calculations were made considering  $l_{sp}$  = longitudinal scour hole profile,  $c^b$  = depth-integrated frontal scour hole area, and  $i = 1, \dots, N$  in which  $N$  is the total number of measured cross sections over time. In the absence of suspension, the sediment flux of the scour hole in terms of bedload could be estimated with an accuracy of  $\pm 2D_{50}$ . For further analysis,  $q_b$  was replaced with the dimensionless bedload flux ( $q^*$ ):

$$q^* = q_b / ((\rho_s / \rho - 1) g D_{50}^3)^{1/2} \tag{7}$$

In general,  $q^*$  showed a nonlinear evolution over time irrespective of the hydrograph shape and flow intensity. The relationship of  $q^*$  over the nondimensional time scale could be approximated through a power law relationship and an ordinary least squares estimation with a mean coefficient of determination ( $R^2$ ) equaling 0.83 (Figure 12).

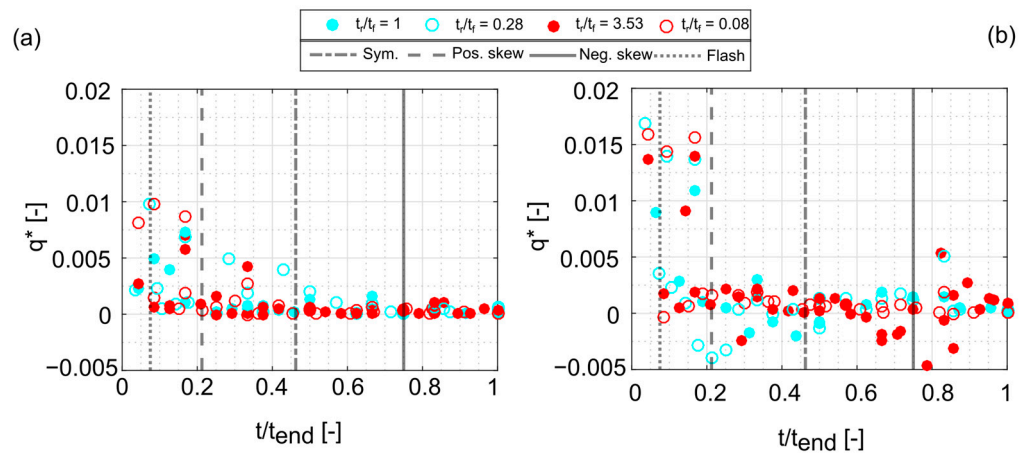


**Figure 12.** Dimensionless bedload ( $q^*$ ) versus dimensionless time scale of experiments ( $t/t_{end}$ ): (a) clear water and (b) general sediment transport.

In clear-water conditions (Figure 12a),  $q^*$  was high in the rising limb ( $t_r$ ) of the hydrographs due to intense scouring and the enlargement of the geometrical length scales at  $d_w/L_o \leq 1.5$ . Afterwards,  $q^*$  significantly decreased proceeding peak flow (vertical grey lines) and reached an almost null value in the falling limb.

For general sediment transport,  $q^*$  turned negative at peak flow for each hydrograph shape, as approaching the bedload sheets refilled the scour hole. Afterwards,  $q^*$  turned positive again, recovering to a bedload comparable to  $q^*$  prior to peak flow, so the scour hole reconstituted to a size comparable to the prepeak flow conditions as the sediment supply into the local scour hole was mitigated (Figure 12b).

An analysis of covariance (F-value = 1.32–1.59,  $p$ -value = 0.02) on the log-transformed values of  $q^*$  and  $t/t_{end}$  revealed that the relationship did not statistically differ amongst the hydrograph shapes at a 95% confidence interval in clear-water conditions and for general sediment transport.

Because the bedload transported out of the frontal local scour hole varied with different unit discharges in different hydraulic scenarios, hysteresis was present in the experimental results. In clear-water conditions, a clockwise hysteresis pattern was present (Figure 13a), while, for general sediment transport, a Figure 8 hysteresis loop was present [90] (Figure 13b).

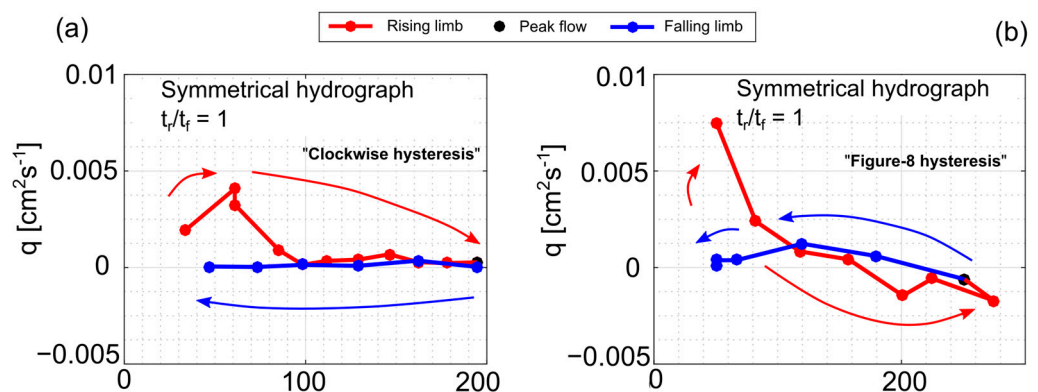


**Figure 13.** Hysteresis pattern: (a) clear water and (b) channel degradation.

The observed hysteresis loops coincided with the field observations on local scouring at logs embedded in sand and affected by different extents of submergence during flood events reported by [91].

5.2. Local Scour Geometry

The enlargement of  $l_s$  and  $w_s$  was triggered by the deepening of  $d_s$  in the inner scour hole, which undermined the scour slopes and induced intermittent gravitational movements at the flanks. In the developing scour holes, segmentation (Figure 3) was visible during the experiments. The inclination of the upper scour slope ( $\Phi$ ) showed a decreasing tendency over time. For  $t/t_{end} \leq 0.25$ ,  $\Phi$  ranged from  $32^\circ$  to  $40^\circ$ , and the frequent sliding of the sediment could be observed. Meanwhile, for  $0.5 > t/t_{end} \leq 1$ ,  $\Phi$  was  $23^\circ$  to  $32^\circ$ , and the gravitational movements at the slope eased.

Over the same time, the span of the scour hole bottom ( $S_b$ ) expanded from  $S_b/L_o \approx 0.3$  to  $S_b/L_o \approx 0.6$ . The enlargement of  $S_b$  was attributed to the expansion of the HV during scouring, which has been documented in an experimental study on bridge pier scouring reported by [51]. The expansion of the HV decreased the shear stress beneath the vortex for sediment mobilization and contributed to the asymptotical approach of an equilibrium condition of the scour depth [57,60].

By neglecting different hydrograph shapes and durations, a monotonic increase and covariation of  $l_s/L_o$  and  $w_s/L_o$  with  $d_s/L_o$  was present in clear-water conditions and for general sediment transport in all the experimental series that could be estimated by

$$l_s/L_o = 1.79 d_s/L_o \tag{8}$$

$$w_s/L_o = 3.89 d_s/L_o \tag{9}$$

with a coefficient of determination ( $R^2$ ) = 0.88 (Figure 14a) and 0.82 (Figure 14b), respectively.

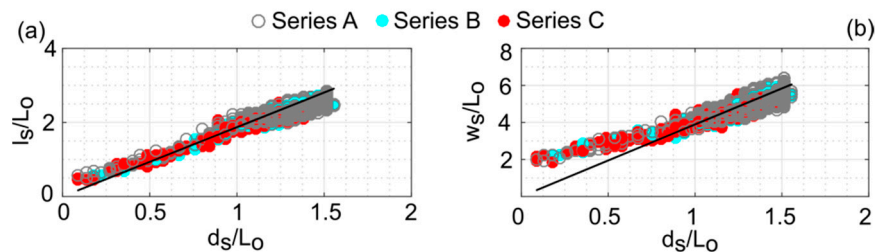


Figure 14. Dependence of nondimensional geometrical length scales on nondimensional scour hole depth in different experimental series: (a) scour hole length and (b) scour hole width.

The longitudinal and horizontal cross sections of the scour hole were scaled with the corresponding dimensions of  $d_s$  and  $l_s$  in order to preserve the collinearity of the distances and angles (i.e., three or more points initially lying on a line still lie on a line after transformation) [92]. The scaled cross sections of the scour hole superimposed and collapsed into a narrow band irrespective of time, which is consistent with the experimental observations reported by [93]. Thus, it is stated that the conical shape of the local scour hole remained constant during local scour evolution. Based on its shape, the evolution of longitudinal and horizontal cross sections over time could be modeled by Gaussian functions [94]:

$$(z + d_s)/d_s = 1.037 e^{-((l_s/x - 1.7138)/0.7463)^2} + 0.6074 e^{-((l_s/x - 0.8417)/0.4782)^2} \tag{10}$$

$$(z + d_s)/d_s = 1.0112 e^{-((w_s/y - 1.0899)/0.64412)^2} + 1.0086 e^{-((w_s/y - 1.1140)/0.5726)^2} \tag{11}$$

with a coefficient of determination ( $R^2$ ) = 0.99 (Figure 15a) and 0.97, respectively (Figure 15b).

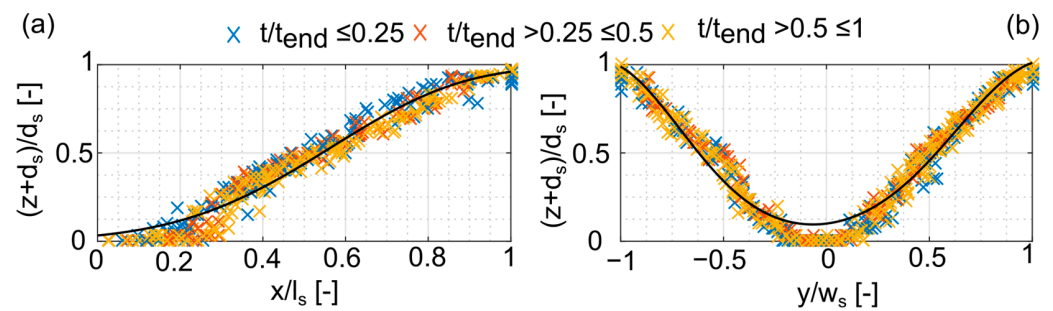


**Figure 15.** Scaled scour hole cross sections at different time intervals: (a) longitudinal ( $l_s$  to  $d_s$ ) and (b) horizontal ( $w_s$  to  $d_s$ ).

By assuming the shape of an inverted frustum cone, the volume of the local scour hole ( $V_s$ ) could be estimated by

$$V_s = (d_s \pi/3) (l_s^2 + S_b \times l_s + S_b^2) \tag{12}$$

In clear-water conditions, irrespective of the hydrograph shape, the normalized local scour hole volume ( $V_s/B^{1/3}$ ) showed reasonable agreement to a mechanistic model proposed by [33] that assesses local scour hole enlargement over time based on

- (i)  $d_s$ ;
- (ii) the cotangent of slope inclination ( $\tan^{-1} \Phi$ );
- (iii)  $S_b$ .

The coefficient of determination ( $R^2$ ) was 0.91 (Figure 16).

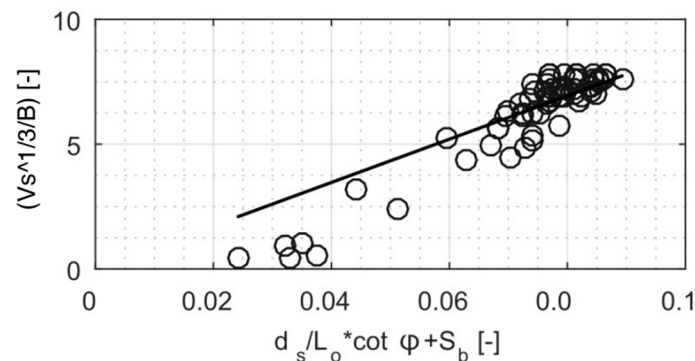


**Figure 16.** Normalized local scour hole volume of present experimental results versus model of local scour hole enlargement [29].

### Geometrical Relationships over Time

The geometrical relationships of the local scour hole ( $d_s/l_s$  and  $d_s/w_s$ ) were not constant over the experimental runtime. In clear-water conditions, irrespective of the hydrograph shape, a piecewise linear pattern was present that was composed of (Figures 17 and 18).

- (i) The considerable enlargement of  $d_s/l_s$  and  $d_s/w_s$  at the beginning of the experiments as  $d_s$  increased quicker than  $l_s$  and  $w_s$ , approaching the maximum value of  $d_s/l_s$  and  $d_s/w_s$ ;
- (ii) The easing of the enlargement and the decreasing of the tendency of  $d_s/l_s$  and  $d_s/w_s$  afterwards as  $d_s$  matured to its finale size, while a slight increase in  $w_s$  occurred.

Quantitatively, the stages were separated by change points that marked instabilities in the slope coefficients ( $\beta_1$ ) during the regression of  $d_s/l_s$  and  $d_s/w_s$  over  $t/t_e$ . Between the change points, the slope coefficients were significantly different irrespective of the hydrograph shape.

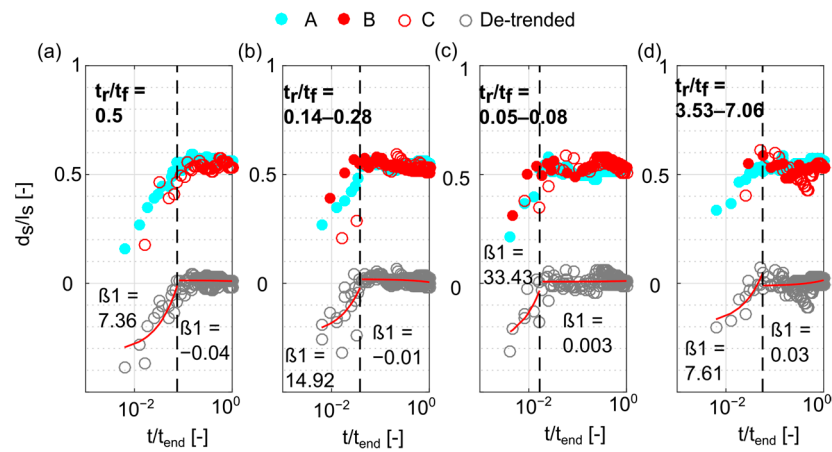


**Figure 17.** Geometrical relationship of  $d_s/l_s$  vs. nondimensional time in clear-water conditions and for different hydrograph shapes: (a) symmetrical, (b) positively skewed, (c) flash flood, and (d) negatively skewed.

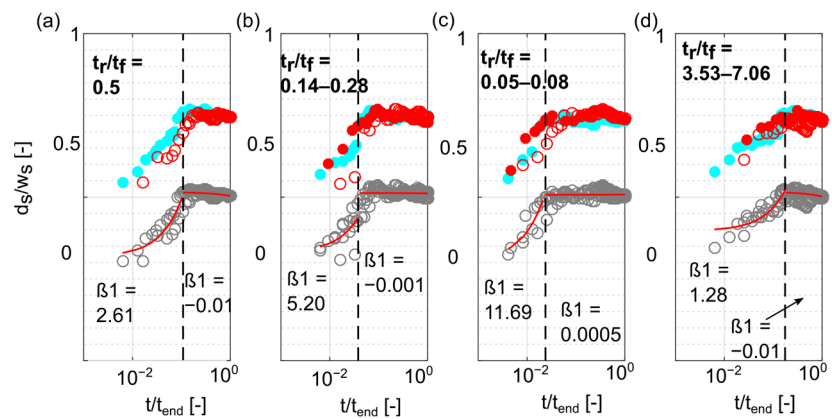


**Figure 18.** Geometrical relationship of  $d_s/w_s$  vs. nondimensional time in clear-water conditions and for different hydrograph shapes: (a) symmetrical, (b) positively skewed, (c) flash flood, and (d) negatively skewed.

Before the change point, over time,  $\beta_1$  was  $\gg 1$ , which corresponded to the conditions described in (i). After the change point,  $\beta_1$  reached near zero or became negative, which corresponded to the processes formulated in (ii). Analyses to derive  $\beta_1$  were performed on the detrended data.

For different hydrograph shapes, in clear-water conditions, the occurrence of change points in  $d_s/l_s$  over  $t/t_{end}$  slightly varied, ranging from  $t/t_{end} = 0.0167$  at  $t_r/t_f = 0.05-0.08$  to  $t/t_{end} = 0.0563$  at  $t_r/t_f = 3.53-7.06$ . For  $d_s/w_s$  over  $t/t_e$ , the change points occurred at  $t/t_{end} = 0.0238$  to  $0.175$ . Thus, it is proposed that two temporal stages can be described based on the geometrical relationships of the local scour hole.

The first stage is characterized by the considerable deepening of the local scour hole. The second stage is characterized by reduced deepening, while the local scour hole then widens. The presence of the two stages can be explained by the expansion of the HV during scouring, which reduced the erosive energy of the vortex and the potential of the HV to further deepen the local scour hole and vice versa [95].

The further enlargement of  $w_s$  was attributed to the convection of the detached shear layers from the legs of the HV1 at the lateral sides of the obstacle, which resulted in the strong amplification of shear stress at the bed as shown by [39,59].

The present observation of the different stages of local scouring corresponds to results reported in [33,51] for local scouring at boulder-like obstacles exposed to long-

lasting ( $t_{\text{end}} = 5760$  min) constant discharge where substantial depth incision occurred for  $t/t_{\text{end}} \leq 0.04$ .

### 5.3. Impact of Hydrograph Chronologies

In addition to the individual runs, the positive, negative, and flash flood hydrographs in Series C ( $t = 120$  min) and scenario 1 were repeated three times in row ( $t_{\text{end}} = 480$  min) to evaluate the impact of the hydrograph chronologies (i.e., the sequences of hydrographs with a certain shape) on local scouring.

After each experimental run, the pump was stopped, and the flume was carefully drained. Afterwards, the flume was filled again to  $d_w = 2$  cm before the pump was started at the  $q$  of the first hydrograph step. The procedure did not cause distortions in the local scour hole (i.e., the collapsing of the local scour hole flanks).

The digital elevation models (DEMs) of the local scour hole after each hydrograph in drained conditions were derived by applying structure-from-motion multiview stereo photogrammetry (SfM-MVS), which can resolve a 3D structure from overlapped images taken from varying perspectives (i.e., camera positions) [96–98]. A comprehensive overview on the SfM-MVS workflow used in the analysis is provided in Appendix B.

Geomorphic changes caused by subsequent flood events were afterwards quantified with DEMs of difference (DoDs). DoDs were generated using Geomorphic Change Detection software (version 7) [99]. Thresholds of change detection (i.e., levels of detection (LoD)) used to evaluate uncertainty were evaluated using standard Gaussian error propagation:

$$\text{LoD} = ((\delta(z)_{\text{DEM } t_1})^2 + (\delta(z)_{\text{DEM } t_2})^2)^{1/2} \quad (13)$$

where  $\delta(z)_{\text{DEM } t_1}$  is the vertical error at time step 1 and where  $\delta(z)_{\text{DEM } t_2}$  is the vertical error at time step 2, respectively. Areas below LoD were considered to be noise, and areas above LoD were interpreted as topographic changes. DoDs could be constructed for a LoD = 0.1 cm.

The experiments of repeated discharge revealed that the local scour hole was persistent over time, while the considerable erosion of the entire area of the local scour hole was present in DoD 1 (Figure 19e). The amount of erosion was decreasing in DoD 2 (Figure 19f). In DoD 3, deposition was dominant due to the sediment reworking at the sediment ridge, which extended in the downstream direction.

The increments of  $d_s$  and  $l_s$  were largest in the rising limb of the first hydrograph for which 80–90% of the dimensions at  $t_{\text{end}}$  were reached. The substantial enlargement of  $d_s$  and  $l_s$  did not occur in the second flood event (i.e., hydrograph II). The geometrical length scales then asymptotically approached their final values at  $t_{\text{end}} = 480$  min irrespective of the hydrograph shape.

However, a slight increase in  $w_s$  was present past hydrograph II for all the considered hydrograph shapes. The size of the geometrical length scales after hydrograph IV (i.e., 480 min) was equal to the size of the  $d_s$ ,  $l_s$ , and  $w_s$  of the Series A experiments with equal experimental durations. Although  $d_s$ ,  $l_s$ , and  $w_s$  were cumulating, it became obvious that local scouring is a history-dependent phenomenon. Thus, a relative change in the geometrical length scales during a subsequent hydrograph event would depend on the  $d_s$ ,  $l_s$ , and  $w_s$  which were reached before the occurrence of the event itself. This attribute was previously described by [30,31] as the so-called memory effect of local scouring.

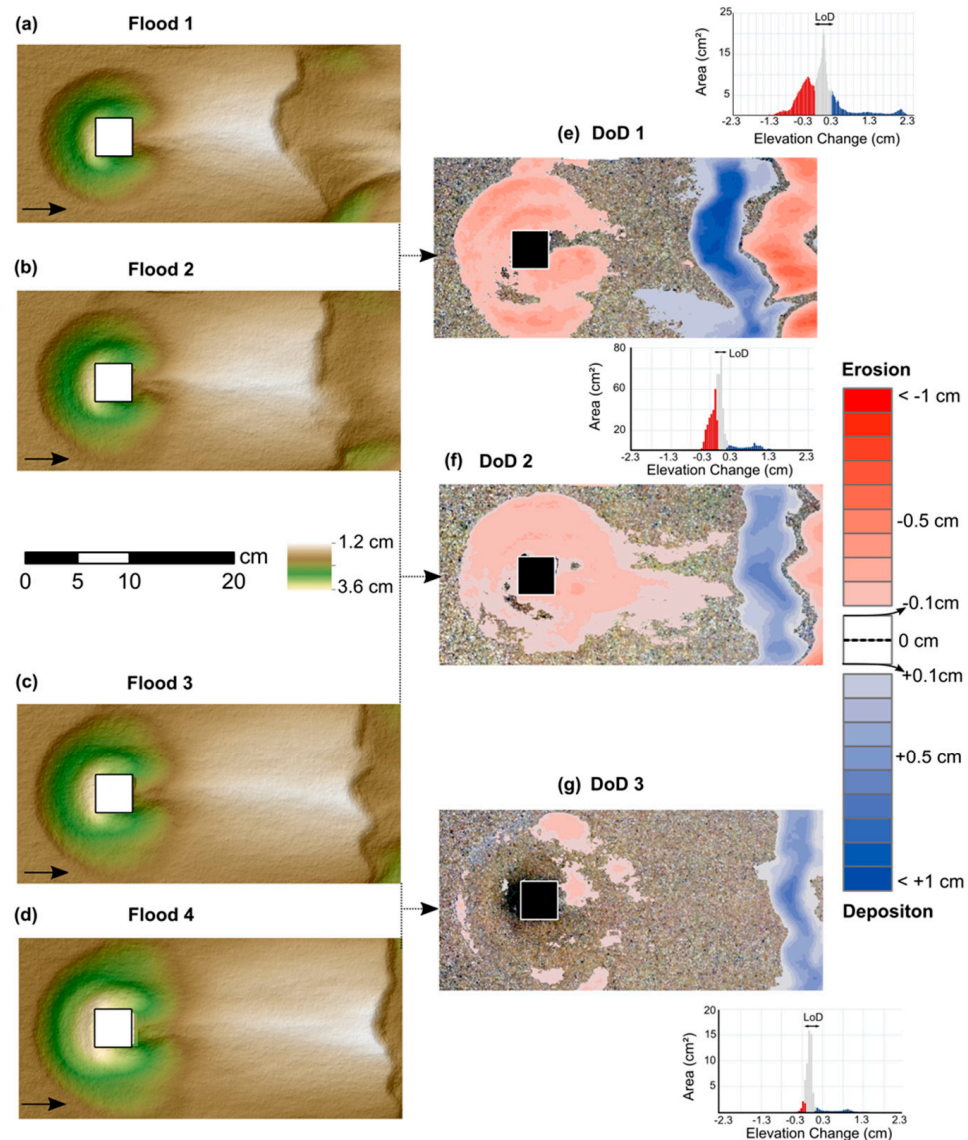


**Figure 19.** Modeled DEMs (a–d) and associated DoDs (e–g) for flash flood hydrographs in clear-water conditions: (a) Flood 1, (b) Flood 2, (c) Flood 3, (d) Flood 4, (e) DoD 1, (f) DoD 2, and (g) DoD 3. Arrows indicate direction of flow.

## 6. Conclusions

Local scouring at an angular obstacle was experimentally investigated for unsteady discharge and variable submergence in obstacle conditions, in clear-water conditions, and for general sediment transport. Opposite to prior studies on sediment trapping in the wake of instream obstacles, this study focused on the local scouring phenomenon. The experiments were designed to mimic local scouring at boulders in ephemeral streams affected by the occurrence of flash floods. Although only simply shaped single-peaked hydrographs were constructed, which are in contrast to the possibly infinite range of the different hydrograph shapes in natural conditions, the following conclusions considering local scouring at boulders in ephemeral streams were drawn:

- Considerable local scouring was attributed to the rising limb of the hydrographs when the flow depth ( $d_w$ ) was comparable to the size of the obstacle ( $L_o$ ), i.e., when  $d_w/L_o \approx 1$ . The obstacle then was unsubmerged, which had paramount impact on the size of the emerging local scour hole in depth ( $d_s$ ), length ( $l_s$ ), and width ( $w_s$ ) because an intense downflow at the obstacle front was present due to a high pressure gradient that, in addition to a strong horseshoe vortex system (HV) at the obstacle base, favored

the scouring processes. Similar conditions are described for scouring at bridge piers. The size of the local scour hole was proportional to the dimensional flow work of the hydrograph ( $W^*$ ) as proposed by [13]. With increasing submergence, in the course of the hydrograph ( $d_w/L_o > 1$ ), local scouring eased the downflow while the HV also weakened. Therefore, it is supposed that, with dependence on the flow depth, the peak flow of a flood might only marginally impact the size of the local scour hole if the obstacle is fully submerged, which is in contrast to bridge pier scouring.

- Up to 80% of the local scour hole size at the end of the experimental runs was reached in only 10% of the experimental runtime, and the shape of a hydrograph in terms of its skewness played an important factor. The steeper the rising limb, the quicker the size of  $d_s$ ,  $l_s$ , and  $w_s$  matured. The enlargement of  $l_s$  and  $w_s$  was therefore attributed to the deepening of the local scour hole, which undermined the local scour hole slopes and induced gravitational movements. A simple mechanistic model was presented that assessed local scour hole volume over time based on the scour depth, the inclination of the local scour hole slopes, and the span of the local scour hole bottom.
- Two temporal evolution stages of the local scour hole were identified based on its geometrical relationships ( $d_s/w_s$  and  $d_s/l_s$ ). It is speculated that the geometrical relationship of preserved local scour holes at boulder obstacles located in ephemeral streams may be used as a length scale to plausibly estimate the minimum duration of the rising limb of a flood hydrograph.
- The experimental runs on the impact of the discharge chronologies in clear-water conditions revealed that local scour holes are transient bed features in the sense that they persist as long as the obstacles that create them are present. However, boulders are mobile, and scouring can cause tilting and the self-burial of the obstacle. Additionally, general sediment transport during floods and the passage of bedforms might cause the disappearance of the entire structure.
- Local scouring is history-dependent on subsequent hydrograph events, and memory effects are present that describe the dependence on the antecedent sizes of  $d_s$ ,  $l_s$ , and  $w_s$ . The greatest impact on the size of the local scour hole was attributed to the rising limb of the initial hydrograph event for which 80–90% of the dimension at the end of the experiments was attained.

However, the validity of the experimental results is restricted to the case of local scouring at a solitary boulder-like obstacle. If an array of boulders is present, the boulder spacing is supposed to be a key variable that has an effect on the flow field and sediment transport processes and vice versa. Therefore, future research should focus on the impact of boulder spacing on local scouring processes and the bed shear stress distribution within the array under variable boulder spacing. Insights into the latter would allow for the physically based correction of the bed shear stress used in the traditional bedload transport formulae in the presence of boulder arrays.

**Author Contributions:** Conceptualization, O.S.; methodology, O.S.; software, O.S.; validation, O.S.; formal analysis, O.S.; investigation, O.S.; resources, J.H.; data curation, O.S.; writing—original draft preparation, O.S.; writing—review and editing, O.S.; visualization, O.S.; supervision, O.S. All authors have read and agreed to the published version of the manuscript.

**Funding:** This research received no external funding.

**Data Availability Statement:** The full experimental dataset is available via the via the Havard dataverse repository: <https://doi.org/10.7910/DVN/EYQP2U>.

**Conflicts of Interest:** The authors declare no conflict of interest.

## Abbreviations

B	Channel cross section (L)
$d_s$	Local scour hole depth at the obstacle front (L)
$d_s/L_o$	Nondimensional scour depth (-)
$d_{sed}$	Thickness of the bed layer (L)
$d_{sed}/L_o$	Relative thickness of the bed layer (-)
$d_w$	Flow depth (L)
$d_w/L_o$	Submergence ratio (-)
$D_{50}$	Median grain diameter of the bed sediment (L)
Fr	Froude number (-)
g	Gravitational acceleration ( $LT^{-2}$ )
$h_o$	Height of the obstacle (L)
HV	Horseshoe vortex system
HV1	Primary horseshoe vortex
HV2	Secondary horseshoe vortex
$L_o$	Effective obstacle size ( $h_o^{2/3} w_o^{1/3}$ ) (-)
$l_e$	Length of obstacle (L)
$L_o/B$	Blockage ratio (-)
$L_o/D_{50}$	Relative sediment coarseness (-)
$l_s$	Local scour hole frontal length (L)
Mb	Indicator for the mobility of a boulder-like obstruction due to tilting (-)
q	Discharge per unit width ( $L^2T^{-1}$ )
$q^b$	Bedload flux out of the local scour hole ( $L^2T^{-1}$ )
$q_p$	Unit discharge at peak flow ( $L^2T^{-1}$ )
$q^*$	Dimensionless bedload flux (-)
Re	Reynolds number (-)
$S_b$	Scour hole bottom (-)
Sh	Hydrodynamic shape of a body ( $L_o/l_e$ )
t	Time (T)
$t_e$	Time scale to reach equilibrium (T)
$t_{end}$	Overall runtime of experimental hydrographs
$t_f$	Duration of the rising limb of experimental hydrographs
$t_r$	Duration of the falling limb of experimental hydrographs
$U_c$	Critical mean approach flow velocity for the entrainment of bed sediment ( $LT^{-1}$ )
$u_c^*$	Critical shear velocity ( $LT^{-1}$ )
$U_m$	Mean approach flow velocity ( $LT^{-1}$ )
$U_m/U_c$	Flow intensity
$U_m/g \times L_o^{1/2}$	Obstacle Froude number ( $Fr_o$ ) (-)
$U_m \times L_o/\nu$	Obstacle Reynolds number ( $Re_o$ ) (-)
$V_s$	Volume of the local scour hole ( $L^3$ )
$W^*$	Dimensionless effective flow work (-)
$w_o$	Obstacle width (L)
$w_s$	Local scour hole frontal width (L)
x	Longitudinal streamwise direction in a local Cartesian coordinate system
y	Perpendicular to streamwise direction in a local Cartesian coordinate system
z	Vertical direction in a local Cartesian coordinate system
$\Phi$	Angle of slopes (-)
$\Phi_{crit}$	Critical angle of repose (-)
$\nu$	Kinematic viscosity ( $L^2T^{-1}$ )
$\rho$	Water density ( $ML^{-3}$ )
$\rho_s$	Sediment density ( $ML^{-3}$ )
$\sigma_G$	Gradation coefficient of sediment ( $D_{84}/D_{16}^{1/2}$ (-))

## Appendix A

**Table A1.** Duration of discharge intervals in experimental hydrographs in Series A/B/C.

Interval (n)	Symmetrical ( $t_r/t_f = 1$ )	Positively Skewed ( $t_r/t_f = 0.28$ )	Negatively Skewed ( $t_r/t_f = 3.53$ )	Flash Flood ( $t_r/t_f = 0.08$ )
1	37/18/9 min	17/4/4 min	60/30/15 min	6/1/1 min
2	37/18/9 min	17/4/4 min	60/30/15 min	6/1/1 min
3	37/18/9 min	17/4/4 min	60/30/15 min	6/1/1 min
4	37/18/9 min	17/4/4 min	60/30/15 min	6/1/1 min
5	37/18/9 min	17/4/4 min	60/30/15 min	6/1/1 min
6	37/18/9 min	17/4/4 min	60/30/15 min	6/1/1 min
7	36/18/9 min	18/4/4 min	18/4/4 min	6/1/1 min
8	37/18/9 min	100/30/15 min	17/4/4 min	73/33/18 min
9	37/18/9 min	100/30/15 min	17/4/4 min	73/33/18 min
10	37/18/9 min	100/30/15 min	17/4/4 min	73/33/18 min
11	37/18/9 min	100/30/15 min	17/4/4 min	73/33/18 min
12	37/18/9 min	100/30/15 min	17/4/4 min	73/33/18 min
13	37/18/9 min	100/30/15 min	17/4/4 min	73/33/18 min

$U_c$  was estimated for different  $d_w$  values by

$$U_c = 5.75 \log_{10} (5.53 d_w / D_{50}) u_c^* \quad (A1)$$

where  $u_c^*$  is the critical shear velocity ( $LT^{-1}$ ), which was estimated by

$$u_c^* = (0.0115 + 0.0125) D_{50}^{1/4} \quad (0.1 \text{ mm} < D_{50} < 1 \text{ mm}) \quad (A2)$$

## Appendix B

The images were acquired using a Panasonic Lumix DMC-G5 (DSLM) camera with a 4/3" (17.3 × 13.0 mm) 16 megapixel image sensor and a Lumix G-Vario 14–42 mm zoom lens set at a 21 mm focal length for minimal image distortion (35 mm full frame equivalent) [100,101], capturing images at a 4608 × 3072 pixel size and at a 52° field of view. The camera was mounted on a cart ~60 cm above the flume, which corresponds to a ground sampling distance of 0.1 mm/pixel. By moving the cart along the longitudinal and horizontal axis of the flume, nadir images (i.e., pointing below a particular direction) were captured at ≥80% side and forward overlap over the area of interest (~30 × 50 cm). Additionally, images at an oblique angle (~45° off-nadir imagery) were taken to enhance capturing the steep features of the morphology (i.e., the local scour hole). After each hydrograph, a complete data set consisted of ≥95 images captured in ≤10 min. Prior to taking images, eight ground control points (GCPs) were distributed throughout the area of interest, which consisted of coded circles with a 4 cm diameter. Target centroids were measured with the measurement technique described above to obtain the x-/y-/z-coordinates.

For processing, PhotoScan software (version 1.2.6) was utilized. The SfM-MVS workflow is an iterative process that comprises of the following: (i) It includes photo alignment using a point-matching algorithm that detects key points in overlapping images and solves for the camera position and camera lens parameters; the alignment accuracy was set to 'high', and pair selection was disabled (key point limit of 40,000 and tie point limit of 1000), identifying >1500 key points in each photoset. (ii) It includes georeferencing based on 2/3 of the GCPs (the remaining GCPs were used for the accuracy assessment) that optimizes the alignment and refines the camera locations by minimizing the error between the modeled

locations and measured locations; according to [101,102], the mean error (ME) is used to estimate the accuracy, the mean absolute error (MAE) is used to estimate the nondirectional height differences, and the standard deviations (SD) are used to estimate the precision. This yielded ME =  $-0.003$  m (x-axis),  $-0.001$  m (y-axis), and  $0.001$  m (z-axis); MAE =  $0.005$  m (x-axis),  $0.003$  m (y-axis), and  $0.0007$  m (z-axis); and SD =  $0.009$  m (x-axis),  $0.004$  m (y-axis), and  $-0.001$  m (z-axis). (iii) It includes the modeling of dense point clouds based on the camera locations and multiview stereo reconstruction, generating dense clouds with  $>8 \times 10^6$  points for each dataset; (iv) DEM generation based on dense point clouds at a  $0.2$  mm/pixel (subgrain size) resolution was used in each dataset to enable comparison.

## References

- Richardson, P.D. The Generation of Scour Marks Near Obstacles. *SEPM JSR* **1968**, *38*, 965–970. [[CrossRef](#)]
- Allen, J.R.L. *Sedimentary Structures: Their Character and Physical Basis*, unabridged one-volume ed.; Elsevier: Amsterdam, The Netherlands, 1984; ISBN 0444422323.
- Breusers, H.N.C.; Raudkivi, A.J. *Scouring*; Balkema: Rotterdam, The Netherlands, 1991; ISBN 9061919835.
- Melville, B.W.; Coleman, S.E. *Bridge Scour*; Water Resources Publications: Highlands Ranch, CO, USA, 2000; ISBN 1887201181.
- Ettema, R.; Constantinescu, G.; Melville, B. *Evaluation of Bridge Scour Research: Pier Scour Processes and Predictions*; Transportation Research Board: Washington, DC, USA, 2011; ISBN 978-0-309-43531-4.
- Pizarro, A.; Manfreda, S.; Tubaldi, E. The Science behind Scour at Bridge Foundations: A Review. *Water* **2020**, *12*, 374. [[CrossRef](#)]
- Chiew, Y.-M. Mechanics of Local Scour Around Submarine Pipelines. *J. Hydraul. Eng.* **1990**, *116*, 515–529. [[CrossRef](#)]
- Sumer, B.M.; Fredsøe, J. *The Mechanics of Scour in the Marine Environment*, Reprinted; World Scientific Publishing: Singapore, 2005; ISBN 9810249306.
- Herget, J.; Schütte, F.; Klosterhalfen, A. Empirical modelling of outburst flood hydrographs. *Zeit. Geo. Supp.* **2015**, *59*, 177–198. [[CrossRef](#)]
- Collischonn, W.; Fleischmann, A.; Paiva, R.C.D.; Mejia, A. Hydraulic Causes for Basin Hydrograph Skewness. *Water Resour. Res.* **2017**, *53*, 10603–10618. [[CrossRef](#)]
- Link, O.; Castillo, C.; Pizarro, A.; Rojas, A.; Ettmer, B.; Escauriaza, C.; Manfreda, S. A model of bridge pier scour during flood waves. *J. Hydraul. Res.* **2017**, *55*, 310–323. [[CrossRef](#)]
- Link, O.; García, M.; Pizarro, A.; Alcayaga, H.; Palma, S. Local Scour and Sediment Deposition at Bridge Piers during Floods. *J. Hydraul. Eng.* **2020**, *146*, 4020003. [[CrossRef](#)]
- Pizarro, A.; Ettmer, B.; Manfreda, S.; Rojas, A.; Link, O. Dimensionless Effective Flow Work for Estimation of Pier Scour Caused by Flood Waves. *J. Hydraul. Eng.* **2017**, *143*, 6017006. [[CrossRef](#)]
- Bombar, G. Scour Evolution Around Bridge Piers Under Hydrographs with High Unsteadiness. *Iran. J. Sci. Technol. Trans. Civ. Eng.* **2020**, *44*, 325–337. [[CrossRef](#)]
- Tsakiris, A.G.; Papanicolaou, A.N.T.; Hajimirzaie, S.M.; Buchholz, J.H.J. Influence of collective boulder array on the surrounding time-averaged and turbulent flow fields. *J. Mt. Sci.* **2014**, *11*, 1420–1428. [[CrossRef](#)]
- Shamloo, H.; Rajaratnam, N.; Katopodis, C. Hydraulics of simple habitat structures. *J. Hydraul. Res.* **2001**, *39*, 351–366. [[CrossRef](#)]
- Lacey, R.W.J.; Rennie, C.D. Laboratory Investigation of Turbulent Flow Structure around a Bed-Mounted Cube at Multiple Flow Stages. *J. Hydraul. Eng.* **2012**, *138*, 71–84. [[CrossRef](#)]
- Sadeque, M.A.; Rajaratnam, N.; Loewen, M.R. Flow around Cylinders in Open Channels. *J. Eng. Mech.* **2008**, *134*, 60–71. [[CrossRef](#)]
- Sadeque, M.A.; Rajaratnam, N.; Loewen, M.R. Effects of Bed Roughness on Flow around Bed-Mounted Cylinders in Open Channels. *J. Eng. Mech.* **2009**, *135*, 100–110. [[CrossRef](#)]
- Papanicolaou, A.N.; Kramer, C. Flow and Sediment Laboratory Measurements over Unsubmerged Roughness Elements. In Proceedings of the World Environmental and Water Resources Congress 2006, Omaha, NE, USA, 21–25 May 2006; Graham, R., Ed.; American Society of Civil Engineers: Reston, VA, USA, 2006; Volume 05192006, pp. 1–8, ISBN 978-0-7844-0856-8.
- Papanicolaou, A.N.; Tsakiris, A.G.; Kramer, C.M. Effects of relative submergence on flow and sediment patterns around clasts. In *River Flow 2010, Proceedings of the [5th] International Conference on Fluvial Hydraulics, Braunschweig, Germany, 8–10 June 2010*; Dittrich, A., Ed.; Bundesanst für Wasserbau: Karlsruhe, Germany, 2010; pp. 793–799, ISBN 978-3-939230-00-7.
- Hajimirzaie, S.M.; Wojcik, C.J.; Buchholz, J.H.J. The role of shape and relative submergence on the structure of wakes of low-aspect-ratio wall-mounted bodies. *Exp. Fluids* **2012**, *53*, 1943–1962. [[CrossRef](#)]
- Hajimirzaie, S.M.; Buchholz, J.H.J. Flow dynamics in the wakes of low-aspect-ratio wall-mounted obstacles. *Exp. Fluids* **2013**, *54*, 1616. [[CrossRef](#)]
- Reid, I.; Laronne, J.B.; Powell, D.M. Flash-flood and bedload dynamics of desert gravel-bed streams. *Hydrol. Process.* **1998**, *12*, 543–557. [[CrossRef](#)]
- Powell, D.M. Dryland rivers: Processes and forms. In *Geomorphology of Desert Environments*; Parsons, A.J., Abrahams, A.D., Eds.; Springer: Dordrecht, The Netherlands, 2009; pp. 333–373, ISBN 978-1-4020-5718-2.

26. Calle, M.; Alho, P.; Benito, G. Channel dynamics and geomorphic resilience in an ephemeral Mediterranean river affected by gravel mining. *Geomorphology* **2017**, *285*, 333–346. [[CrossRef](#)]
27. Shobe, C.M.; Turowski, J.M.; Nativ, R.; Glade, R.C.; Bennett, G.L.; Dini, B. The role of infrequently mobile boulders in modulating landscape evolution and geomorphic hazards. *Earth-Sci. Rev.* **2021**, *220*, 103717. [[CrossRef](#)]
28. Alexander, J.; Cooker, M.J. Moving boulders in flash floods and estimating flow conditions using boulders in ancient deposits. *Sedimentology* **2016**, *63*, 1582–1595. [[CrossRef](#)]
29. Herget, J.; Euler, T.; Roggenkamp, T.; Zemke, J. Obstacle marks as palaeohydraulic indicators of Pleistocene megafloods. *Hydrol. Res.* **2013**, *44*, 300–317. [[CrossRef](#)]
30. Tubaldi, E.; Macorini, L.; Izzuddin, B.A.; Manes, C.; Laio, F. A framework for probabilistic assessment of clear-water scour around bridge piers. *Struct. Saf.* **2017**, *69*, 11–22. [[CrossRef](#)]
31. Pizarro, A.; Tubaldi, E. Quantification of Modelling Uncertainties in Bridge Scour Risk Assessment under Multiple Flood Events. *Geosciences* **2019**, *9*, 445. [[CrossRef](#)]
32. Baynes, E.R.C.; van de Lageweg, W.I.; McLelland, S.J.; Parsons, D.R.; Aberle, J.; Dijkstra, J.; Henry, P.-Y.; Rice, S.P.; Thom, M.; Moulin, F. Beyond equilibrium: Re-evaluating physical modelling of fluvial systems to represent climate changes. *Earth-Sci. Rev.* **2018**, *181*, 82–97. [[CrossRef](#)]
33. Schlömer, O.; Grams, P.E.; Buscombe, D.; Herget, J. Geometry of obstacle marks at instream boulders—Integration of laboratory investigations and field observations. *Earth Surf. Process. Landf.* **2020**, *46*, 659–679. [[CrossRef](#)]
34. Euler, T.; Herget, J. Controls on local scour and deposition induced by obstacles in fluvial environments. *CATENA* **2012**, *91*, 35–46. [[CrossRef](#)]
35. Euler, T.; Herget, J. Obstacle-Reynolds-number based analysis of local scour at submerged cylinders. *J. Hydraul. Res.* **2011**, *49*, 267–271. [[CrossRef](#)]
36. Douglas, J.F.; Gasiorek, J.M.; Swaffield, J.A. *Fluid Mechanics*, 4th ed.; Prentice Hall: Harlow, UK, 2001; ISBN 0582414768.
37. Rennie, S.E.; Brandt, A.; Friedrichs, C.T. Initiation of motion and scour burial of objects underwater. *Ocean Eng.* **2017**, *131*, 282–294. [[CrossRef](#)]
38. Escauriaza, C.; Sotiropoulos, F. Initial stages of erosion and bed form development in a turbulent flow around a cylindrical pier. *J. Geophys. Res.* **2011**, *116*, 671. [[CrossRef](#)]
39. Kirkil, G.; Constantinescu, G. Flow and turbulence structure around an in-stream rectangular cylinder with scour hole. *Water Resour. Res.* **2010**, *46*, W11549. [[CrossRef](#)]
40. Radice, A.; Tran, C.K. Study of sediment motion in scour hole of a circular pier. *J. Hydraul. Res.* **2012**, *50*, 44–51. [[CrossRef](#)]
41. Chen, Q.; Qi, M.; Zhong, Q.; Li, D. Experimental study on the multimodal dynamics of the turbulent horseshoe vortex system around a circular cylinder. *Phys. Fluids* **2017**, *29*, 15106. [[CrossRef](#)]
42. Li, J.; Qi, M.; Fuhrman, D.R.; Chen, Q. Influence of turbulent horseshoe vortex and associated bed shear stress on sediment transport in front of a cylinder. *Exp. Therm. Fluid Sci.* **2018**, *97*, 444–457. [[CrossRef](#)]
43. Link, O.; González, C.; Maldonado, M.; Escauriaza, C. Coherent structure dynamics and sediment particle motion around a cylindrical pier in developing scour holes. *Acta Geophys.* **2012**, *60*, 1689–1719. [[CrossRef](#)]
44. Ettema, R.; Yoon, B.; Nakato, T.; Muste, M. A review of scour conditions and scour-estimation difficulties for bridge abutments. *KSCE J. Civ. Eng.* **2004**, *8*, 643–650. [[CrossRef](#)]
45. Okamoto, S.; Sunabashiri, Y. Vortex Shedding From a Circular Cylinder of Finite Length Placed on a Ground Plane. *J. Fluids Eng.* **1992**, *114*, 512–521. [[CrossRef](#)]
46. Pattenden, R.J.; Turnock, S.R.; Zhang, X. Measurements of the flow over a low-aspect-ratio cylinder mounted on a ground plane. *Exp. Fluids* **2005**, *39*, 10–21. [[CrossRef](#)]
47. Dey, S.; Sarkar, S.; Bose, S.K.; Tait, S.; Castro-Organ, O. Wall-Wake Flows Downstream of a Sphere Placed on a Plane Rough Wall. *J. Hydraul. Eng.* **2011**, *137*, 1173–1189. [[CrossRef](#)]
48. Hajimirzaie, S.M.; Tsakiris, A.G.; Buchholz, J.H.J.; Papanicolaou, A.N. Flow characteristics around a wall-mounted spherical obstacle in a thin boundary layer. *Exp. Fluids* **2014**, *55*, 1762. [[CrossRef](#)]
49. Papanicolaou, A.N.; Kramer, C.M.; Tsakiris, A.G.; Stoesser, T.; Bomminayuni, S.; Chen, Z. Effects of a fully submerged boulder within a boulder array on the mean and turbulent flow fields: Implications to bedload transport. *Acta Geophys.* **2012**, *60*, 1502–1546. [[CrossRef](#)]
50. Euler, T.; Herget, J.; Schlömer, O.; Benito, G. Hydromorphological processes at submerged solitary boulder obstacles in streams. *CATENA* **2017**, *157*, 250–267. [[CrossRef](#)]
51. Schlömer, O. Morphodynamic relation of obstacle marks at boulder-like obstructions in time. In *River Flow 2020, Proceedings of the 10th Conference on Fluvial Hydraulics, Delft, The Netherlands, 7–10 July 2020*; Uijtewaal, W.S.J., Ed.; CRC Press/Balkema: Leiden, The Netherlands, 2020; pp. 719–727, ISBN 9780367627737.
52. Hajimirzaie, S.M. Experimental Observations on Flow Characteristics around a Low-Aspect-Ratio Wall-Mounted Circular and Square Cylinder. *Fluids* **2023**, *8*, 32. [[CrossRef](#)]
53. da Silva, B.L.; Sumner, D.; Bergstrom, D.J. Mean and Dynamic Aspects of the Wakes of a Surface-Mounted Cube and Block. *J. Fluids Eng.* **2022**, *144*, 011302. [[CrossRef](#)]
54. da Silva, B.L.; Hahn, D.G.H.; Sumner, D.; Bergstrom, D.J. Mean wake and aerodynamic forces for surface-mounted finite-height square prisms of very small aspect ratio. *Phys. Fluids* **2022**, *34*, 115118. [[CrossRef](#)]

55. Fu, H.; Rockwell, D. Shallow flow past a cylinder: Transition phenomena at low Reynolds number. *J. Fluid Mech.* **2005**, *540*, 75. [[CrossRef](#)]
56. Sumner, D.; Heseltine, J.L.; Dansereau, O.J.P. Wake structure of a finite circular cylinder of small aspect ratio. *Exp. Fluids* **2004**, *37*, 720–730. [[CrossRef](#)]
57. Dargahi, B. Controlling Mechanism of Local Scouring. *J. Hydraul. Eng.* **1990**, *116*, 1197–1214. [[CrossRef](#)]
58. Chen, Q.; Yang, Z.; Wu, H. Evolution of Turbulent Horseshoe Vortex System in Front of a Vertical Circular Cylinder in Open Channel. *Water* **2019**, *11*, 2079. [[CrossRef](#)]
59. Kirkil, G.; Constantinescu, S.G.; Ettema, R. Coherent Structures in the Flow Field around a Circular Cylinder with Scour Hole. *J. Hydraul. Eng.* **2008**, *134*, 572–587. [[CrossRef](#)]
60. Unger, J.; Hager, W.H. Down-flow and horseshoe vortex characteristics of sediment embedded bridge piers. *Exp. Fluids* **2006**, *42*, 1–19. [[CrossRef](#)]
61. Muzzammil, M.; Gangadhariah, T. The mean characteristics of horseshoe vortex at a cylindrical pier. *J. Hydraul. Res.* **2003**, *41*, 285–297. [[CrossRef](#)]
62. Guan, D.; Chiew, Y.-M.; Wei, M.; Hsieh, S.-C. Characterization of horseshoe vortex in a developing scour hole at a cylindrical bridge pier. *Int. J. Sediment Res.* **2019**, *34*, 118–124. [[CrossRef](#)]
63. Paik, J.; Escauriaza, C.; Sotiropoulos, F. On the bimodal dynamics of the turbulent horseshoe vortex system in a wing-body junction. *Phys. Fluids* **2007**, *19*, 45107. [[CrossRef](#)]
64. Kirkil, G.; Constantinescu, G. Effects of cylinder Reynolds number on the turbulent horseshoe vortex system and near wake of a surface-mounted circular cylinder. *Phys. Fluids* **2015**, *27*, 75102. [[CrossRef](#)]
65. Radice, A.; Porta, G.; Franzetti, S. Analysis of the time-averaged properties of sediment motion in a local scour process. *Water Resour. Res.* **2009**, *45*, W03401. [[CrossRef](#)]
66. Schlömer, O.; Herget, J.; Euler, T. Boundary condition control of fluvial obstacle mark formation—Framework from a geoscientific perspective. *Earth Surf. Process. Landf.* **2020**, *45*, 189–206. [[CrossRef](#)]
67. Kothyari, U.C.; Garde, R.C.J.; Raju, K.G.R. Temporal Variation of Scour Around Circular Bridge Piers. *J. Hydraul. Eng.* **1992**, *118*, 1091–1106. [[CrossRef](#)]
68. Simarro, G.; Fael, C.M.S.; Cardoso, A.H. Estimating Equilibrium Scour Depth at Cylindrical Piers in Experimental Studies. *J. Hydraul. Eng.* **2011**, *137*, 1089–1093. [[CrossRef](#)]
69. Oliveto, G.; Hager, W.H. Temporal Evolution of Clear-Water Pier and Abutment Scour. *J. Hydraul. Eng.* **2002**, *128*, 811–820. [[CrossRef](#)]
70. Melville, B.W.; Chiew, Y.-M. Time Scale for Local Scour at Bridge Piers. *J. Hydraul. Eng.* **1999**, *125*, 59–65. [[CrossRef](#)]
71. Sonin, A.A. A generalization of the Pi-theorem and dimensional analysis. *Proc. Natl. Acad. Sci. USA* **2004**, *101*, 8525–8526. [[CrossRef](#)] [[PubMed](#)]
72. Manes, C.; Coscarella, F.; Rogers, A.; Gaudio, R. Viscosity effects on local scour around vertical structures in clear-water conditions. *E3S Web Conf.* **2018**, *40*, 3038. [[CrossRef](#)]
73. Belmonte, A.M.C.; Segura Beltrán, F. Flood events in Mediterranean ephemeral streams (ramblas) in Valencia region, Spain. *CATENA* **2001**, *45*, 229–249. [[CrossRef](#)]
74. Mao, L. The effect of hydrographs on bed load transport and bed sediment spatial arrangement. *J. Geophys. Res.* **2012**, *117*, F03024. [[CrossRef](#)]
75. López, G.; Teixeira, L.; Ortega-Sánchez, M.; Simarro, G. Estimating Final Scour Depth under Clear-Water Flood Waves. *J. Hydraul. Eng.* **2014**, *140*, 328–332. [[CrossRef](#)]
76. Waters, K.A.; Curran, J.C. Linking bed morphology changes of two sediment mixtures to sediment transport predictions in unsteady flows. *Water Resour. Res.* **2015**, *51*, 2724–2741. [[CrossRef](#)]
77. Nakagawa, H.; Nezu, I. *Turbulence in Open Channel Flows*, 1st ed.; CRC Press: Rotterdam, The Netherlands, 1993; ISBN 9789054101185.
78. Rogers, A.; Manes, C.; Tsuzaki, T. Measuring the geometry of a developing scour hole in clear-water conditions using underwater sonar scanning. *Int. J. Sediment Res.* **2020**, *35*, 105–114. [[CrossRef](#)]
79. Bouratsis, P.; Diplas, P.; Dancey, C.L.; Apsilidis, N. Quantitative Spatio-Temporal Characterization of Scour at the Base of a Cylinder. *Water* **2017**, *9*, 227. [[CrossRef](#)]
80. Dey, S.; Raikar, R.V.; Roy, A. Scour at Submerged Cylindrical Obstacles under Steady Flow. *J. Hydraul. Eng.* **2008**, *134*, 105–109. [[CrossRef](#)]
81. Sarkar, A. Scour and flow around submerged structures. *Proc. Inst. Civ. Eng. Water Manag.* **2014**, *167*, 65–78. [[CrossRef](#)]
82. Du, S.; Liang, B. Comparisons of Local Scouring for Submerged Square and Circular Cross-Section Piles in Steady Currents. *Water* **2019**, *11*, 1820. [[CrossRef](#)]
83. Lu, J.-Y.; Shi, Z.-Z.; Hong, J.-H.; Lee, J.-J.; Raikar, R.V. Temporal Variation of Scour Depth at Nonuniform Cylindrical Piers. *J. Hydraul. Eng.* **2011**, *137*, 45–56. [[CrossRef](#)]
84. Gjunsburgs, B.; Jaudzems, G.; Govša, J. Hydrograph Shape Impact on the Scour Development with Time at Engineering Structures in River Flow. *Constr. Sci.* **2010**, *11*, 6–12.
85. Tabarestani, M.K.; Zarrati, A.R. Local scour calculation around bridge pier during flood event. *KSCE J. Civ. Eng.* **2017**, *21*, 1462–1472. [[CrossRef](#)]

86. Chang, W.-Y.; Lai, J.-S.; Yen, C.-L. Evolution of Scour Depth at Circular Bridge Piers. *J. Hydraul. Eng.* **2004**, *130*, 905–913. [[CrossRef](#)]
87. Salamatian, S.A.; Tabarestani, M.K.; Zarrati, A.R. Local scour at cylindrical bridge pier under a flood wave. In *River Flow 2014, Proceedings of the International Conference on Fluvial Hydraulics (River Flow 2014), Lausanne, Switzerland, 3–5 September 2014*; Schleiss, A.J., de Cesare, G., Franca, M.J., Pfister, M., Eds.; CRC Press/Balkema: Boca Raton, FL, USA, 2014; pp. 1387–1391, ISBN 9781138026742.
88. Hong, J.-H.; Chiew, Y.-M.; Yeh, P.-H.; Chan, H.-C. Evolution of Local Pier-Scour Depth with Dune Migration in Subcritical Flow Conditions. *J. Hydraul. Eng.* **2017**, *143*, 4016098. [[CrossRef](#)]
89. Sheppard, D.M.; Miller, W. Live-Bed Local Pier Scour Experiments. *J. Hydraul. Eng.* **2006**, *132*, 635–642. [[CrossRef](#)]
90. Williams, G.P. Sediment concentration versus water discharge during single hydrologic events in rivers. *J. Hydrol.* **1989**, *111*, 89–106. [[CrossRef](#)]
91. Borg, D.; Rutherford, I.; Stewardson, M. The geomorphic and ecological effectiveness of habitat rehabilitation works: Continuous measurement of scour and fill Around large logs in sand-bed streams. *Geomorphology* **2007**, *89*, 205–216. [[CrossRef](#)]
92. Tregnaghi, M.; Marion, A.; Gaudio, R. Affinity and similarity of local scour holes at bed sills. *Water Resour. Res.* **2007**, *43*, W11417. [[CrossRef](#)]
93. Tregnaghi, M.; Marion, A.; Coleman, S. Scouring at Bed Sills as a Response to Flash Floods. *J. Hydraul. Eng.* **2009**, *135*, 466–475. [[CrossRef](#)]
94. Schalko, I.; Lageder, C.; Schmocker, L.; Weitbrecht, V.; Boes, R.M. Laboratory Flume Experiments on the Formation of Spanwise Large Wood Accumulations: I. Effect on Backwater Rise. *Water Resour. Res.* **2019**, *55*, 4854–4870. [[CrossRef](#)]
95. Manes, C.; Brocchini, M. Local scour around structures and the phenomenology of turbulence. *J. Fluid Mech.* **2015**, *779*, 309–324. [[CrossRef](#)]
96. Westoby, M.J.; Brasington, J.; Glasser, N.F.; Hambrey, M.J.; Reynolds, J.M. ‘Structure-from-Motion’ photogrammetry: A low-cost, effective tool for geoscience applications. *Geomorphology* **2012**, *179*, 300–314. [[CrossRef](#)]
97. Smith, M.W.; Carrivick, J.L.; Quincey, D.J. Structure from motion photogrammetry in physical geography. *Prog. Phys. Geogr. Earth Environ.* **2016**, *40*, 247–275. [[CrossRef](#)]
98. Morgan, J.A.; Brogan, D.J.; Nelson, P.A. Application of Structure-from-Motion photogrammetry in laboratory flumes. *Geomorphology* **2017**, *276*, 125–143. [[CrossRef](#)]
99. Wheaton, J.M.; Brasington, J.; Darby, S.E.; Sear, D.A. Accounting for uncertainty in DEMs from repeat topographic surveys: Improved sediment budgets. *Earth Surf. Process. Landf.* **2010**, *35*, 136–156. [[CrossRef](#)]
100. Javernick, L.; Brasington, J.; Caruso, B. Modeling the topography of shallow braided rivers using Structure-from-Motion photogrammetry. *Geomorphology* **2014**, *213*, 166–182. [[CrossRef](#)]
101. James, M.R.; Chandler, J.H.; Eltner, A.; Fraser, C.; Miller, P.E.; Mills, J.P.; Noble, T.; Robson, S.; Lane, S.N. Guidelines on the use of structure-from-motion photogrammetry in geomorphic research. *Earth Surf. Process. Landf.* **2019**, *44*, 2081–2084. [[CrossRef](#)]
102. Lane, S.N.; James, T.D.; Crowell, M.D. Application of Digital Photogrammetry to Complex Topography for Geomorphological Research. *Photogramm. Rec.* **2000**, *16*, 793–821. [[CrossRef](#)]

**Disclaimer/Publisher’s Note:** The statements, opinions and data contained in all publications are solely those of the individual author(s) and contributor(s) and not of MDPI and/or the editor(s). MDPI and/or the editor(s) disclaim responsibility for any injury to people or property resulting from any ideas, methods, instructions or products referred to in the content.